

EXPERIMENTAL FREQUENCY-DEPENDENT ROTORDYNAMIC
COEFFICIENTS FOR A LOAD-ON-PAD, HIGH-SPEED,
FLEXIBLE-PIVOT TILTING-PAD BEARING

A Thesis

by

LUIS EMIGDIO RODRIGUEZ COLMENARES

Submitted to the Office of Graduate Studies of
Texas A&M University
in partial fulfillment of the requirements for the degree of
MASTER OF SCIENCE

May 2004

Major Subject: Mechanical Engineering

EXPERIMENTAL FREQUENCY-DEPENDENT ROTORDYNAMIC
COEFFICIENTS FOR A LOAD-ON-PAD, HIGH-SPEED,
FLEXIBLE-PIVOT TILTING-PAD BEARING

A Thesis

by

LUIS EMIGDIO RODRIGUEZ COLMENARES

Submitted to Texas A&M University
in partial fulfillment of the requirements
for the degree of

MASTER OF SCIENCE

Approved as to style and content by:

Dara W. Childs

(Chair of Committee)

John M. Vance

(Member)

William Schneider

(Member)

James Morgan

(Member)

Dennis L. O'Neal

(Head of Department)

May 2004

Major Subject: Mechanical Engineering

ABSTRACT

Experimental Frequency-Dependent Rotordynamic Coefficients for a Load-On-Pad,
High-Speed, Flexible-Pivot Tilting-Pad Bearing. (May 2004)

Luis Emigdio Rodriguez Colmenares, B.S., Universidad Simón Bolívar, Venezuela
Chair of Advisory Committee: Dr. Dara W. Childs

This thesis provides experimental frequency dependent stiffness and damping coefficient results for a high-speed, lightly loaded, flexible-pivot tilting-pad bearing, with a load-on-pad configuration. Test conditions include four shaft speeds (6000, 9000, 13000 and 16000 rpm), and bearing unit loads from 172 kPa to 690 kPa. The results show that the bearing stiffness is a quadratic function of the frequency of vibration; hence their frequency dependency can be modeled by added-mass terms. The additional degrees of freedom introduced by the pads and the influence of the inertial forces generated in the fluid film account for this frequency dependency. The conventional frequency-dependent stiffness and damping model for tilting-pad bearings is extended with an added-mass matrix to account for the frequency dependency. This approach allows the description of the bearing dynamic characteristics with *frequency-independent* stiffness, damping and added-mass matrices. Experimental results are compared with predictions from the Reynolds equation and from a bulk-flow Navier-Stokes model. Both models produce good predictions of the stiffness and damping coefficients. However, results show that the bulk-flow model is more adequate for predicting the direct added-mass terms because it accounts for the fluid inertial forces. A bulk-flow solution of the Navier-Stokes equations that includes the effects of fluid inertia should be used to calculate the rotordynamic coefficients of a flexible-pivot tilting-bearing.

Static performance measurement results are also detailed. Results include pad metal temperatures, eccentricity-ratios and attitude-angle as a function of bearing load, and estimated power losses.

DEDICATION

This thesis is dedicated to God, who lets us the engineers discover and play with His wonderful creation with a set of rules we like to call “scientific research”.

ACKNOWLEDGEMENTS

I would like to express my gratitude to Dr. Dara Childs, academic advisor, for his support and guidance and for giving me the opportunity to work for him. He helped make my tenure at Texas A&M University a gratifying and learning experience.

I would also like to thank Dr. John Vance, Dr. William Schneider and Dr. James Morgan for serving on my advisory committee. I also thank Dr. Luis San Andres for his support during my first semester at Texas A&M University.

I thank Dr. Fouad Zeidan at Bearings Plus, Inc. for donating the test bearing and the Texas A&M University Turbomachinery Research Consortium for funding the work reported in this thesis.

I want to acknowledge the efforts of fellow student and project mate Adnan Al-Ghasem. It seems that together we learned an important lesson on patience and not losing hope when the facts suggested otherwise. The assistance of the student workers is also appreciated, especially Dustin Pavelek for his immutable willingness to help us. I also thank Stephen Phillips for his help during many aspects of this project. Thanks also to Bugra Ertas (Bearings Plus, Inc.) for answering all of our questions regarding the design of the test bearing.

I thank fellow Turbolab students, Oscar De Santiago, Larry Villasmil, Avijit Bhattacharya, Arthur Picardo, Kai Kai Zhang, Fernando Romero, and many others, for their help, camaraderie and advice. I also thank Eddie Denk for his help with the hardware.

I thank my family for the many words of encouragement and their prayers. I particularly thank my sister for helping me stay healthy during the writing process of this thesis.

These acknowledgements would not be complete if I did not express my thanks to God, who gave me the strength to persevere and placed so many good people in my way during this time in College Station.

TABLE OF CONTENTS

	Page
ABSTRACT	iii
DEDICATION	iv
ACKNOWLEDGEMENTS	v
TABLE OF CONTENTS	vi
LIST OF FIGURES.....	viii
LIST OF TABLES	x
NOMENCLATURE.....	xi
CHAPTER	
I INTRODUCTION	1
II LITERATURE REVIEW	5
III DESCRIPTION OF THE TEST RIG.....	9
Overview	9
Loading Configuration	10
Instrumentation.....	13
Bearing Characteristics	15
IV THEORETICAL BACKGROUND	17
Parameter Identification Model.....	17
Curve-fitting Procedure and Uncertainty Analysis	19
V EXPERIMENTAL PROCEDURE.....	22
Measurement of “Baseline” Dynamic Stiffness.....	23
VI STATIC PERFORMANCE CHARACTERISTICS.....	26
Pad Temperatures	32

CHAPTER	Page
VII DYNAMIC STIFFNESS AND ROTORDYNAMIC COEFFICIENTS.....	35
Bearing Dynamic Stiffness.....	35
Rotordynamic Coefficients	43
Whirl-Frequency Ratio.....	47
VIII BULK-FLOW THEORY PREDICTIONS	48
Foreword	48
Dynamic Stiffness	49
Predicted Rotordynamic Coefficients	56
IX CONCLUSIONS AND RECOMMENDATIONS	59
REFERENCES.....	61
APPENDIX.....	63
VITA	64

LIST OF FIGURES

FIGURE	Page
1 Tilting pad bearing configuration.....	1
2 Flexible-pivot tilting pad bearing.....	2
3 Linearized bearing coefficients.....	3
4 Test rig main test section.....	9
5 Shaker-stinger configuration.....	11
6 Static loader assembly.....	12
7 Bearing stator configuration and instrumentation.....	14
8 Bearing and pad thermocouples location.....	15
9 Coordinate reference frame.....	17
10 Baseline real direct dynamic stiffness.....	23
11 Baseline real cross-coupled dynamic stiffness.....	24
12 Baseline imaginary dynamic stiffness.....	24
13 Pitch stabilizers' static stiffness in the y-direction.....	25
14 Bearing centerline loci plots.....	27
15 Eccentricity ratio versus bearing unit load.....	28
16 Attitude angle versus bearing unit load.....	29
17 Maximum temperature of the loaded pad.....	30
18 Estimated frictional power loss.....	31
19 Pad temperature profiles for 172 kPa and 345 kPa.....	33
20 Pad temperature profiles for 517 kPa and 689 kPa.....	34
21 Real direct dynamic stiffness at 6000 rpm and 689 kPa.....	35
22 Real cross-coupled dynamic stiffness at 6000 rpm and 689 kPa.....	39
23 Imaginary direct dynamic stiffness at 6000 rpm and 689 kPa.....	40
24 Imaginary cross-coupled dynamic stiffness at 6000 rpm and 689 kPa.....	41
25 Bearing stiffness coefficients.....	44
26 Damping bearing coefficients.....	45

FIGURE	Page
27 Bearing added-mass coefficients.....	46
28 Whirl-frequency ratio versus rotational speed and unit load	47
29 Predicted real part of H_{xx} and H_{yy} , 9000 rpm and 689 kPa	50
30 Predicted imaginary part of H_{xx} and H_{yy} , 9000 rpm and 689 kPa	52
31 Predicted real part of H_{xy} and H_{yx} , 9000 rpm and 689 kPa	53
32 Predicted imaginary part of H_{xy} and H_{yx} , 9000 rpm and 689 kPa	55
33 Stiffness coefficients - theory versus experiment	56
34 Damping coefficients - theory versus experiment.....	57
35 Added-mass coefficients - theory versus experiment.....	58

LIST OF TABLES

TABLE	Page
1 Bearing characteristics and operating conditions.....	16
2 Test conditions	22
3 Reynolds numbers for test conditions	36
4 Coefficients of determination for dynamic stiffness at 6000 rpm and 689 kPa.....	42
5 Predicted stiffness and added-mass coefficients, 9000 rpm and 689 kPa.....	51
6 Predicted direct damping coefficients, 9000 rpm and 689 kPa.....	52
7 Predicted cross-coupled stiffness coefficients, 9000 rpm and 689 kPa	54

NOMENCLATURE

A_{ij}	Fourier transforms for the measured stator acceleration. (e.g. A_{ij} is the acceleration in “j” direction, due to an excitation force in the “i” direction) [L/t^2]
C_{ij}	Direct and cross-coupled damping coefficients [$F.t/L$]
ΔC_{ij}	Uncertainty of direct and cross-coupled damping coefficients [$F.t/L$]
C_B	Radial bearing clearance [L]
C_P	Radial pad clearance [L]
c_p	Lubricant specific heat [$F.L/(M.t)$]
D	Bearing diameter [L]
D_{ij}	Fourier transforms for the measured stator relative motion [L]
$e_x e_y$	Bearing equilibrium position in the x and y directions [L]
$e_{x0} e_{y0}$	Initial bearing position (at null load) in the x and y directions [L]
F_{ij}	Fourier transforms for the measured stator force [F]
F_s	Static force applied by pneumatic loader [F]
$f_{bx} f_{by}$	Bearing reaction force component in the x,y direction respectively [F]
$f_x f_y$	Measured excitation force component in the x,y direction [F]
H_{ij}	Direct and cross-coupled dynamic stiffnesses [F/L]
J	Imaginary unit, $\sqrt{-1}$ [-]
K_{ij}	Direct and cross-coupled stiffness coefficients [F/L]
ΔK_{ij}	Uncertainty of direct and cross-coupled stiffness coefficients [F/L]
L	Pad length [L]
M_s	Mass of the stator [M]
M_{ij}	Direct and cross-coupled added-mass coefficients [M]
ΔM_{ij}	Uncertainty of added-mass coefficients [M]
P	Bearing unit load ($\frac{F_s}{LD}$) [F/L^2]

\dot{Q}	Bearing oil supply flow rate [L ³ /t]
R	Bearing radius [L]
Re	Reynolds number, $Re = \frac{\rho C_p R \omega}{\mu}$ [-]
r_{ij}^2	Square of the correlation coefficient [-]
S	Sommerfeld number, $S = \frac{\mu N L D}{W} \left(\frac{R}{C_p} \right)^2$ [-]
T_{in}	Oil inlet temperature [T]
T_{out}	Oil outlet temperature (average of the NDE and DE temperatures) [T]
$\ddot{x}_s \ \ddot{y}_s$	Absolute acceleration of the stator in the x,y direction [L/t ²]
β	Pad pivot angular location (from pad's leading edge) [Angle]
χ	Pad arc angle [Angle]
$\Delta x \ \Delta y$	Relative motion between the rotor and the stator in the x,y directions [L]
ε	Eccentricity ratio [-]
ϕ	Attitude angle measured from the $+y$ axis to the $+x$ axis [Angle]
Λ	Square of the excitation frequency, Ω^2 [(1/t) ²]
ρ	Lubricant density [M/L ³]
ω	Running speed of rotor [1/t]
Ω	Excitation frequency of stator [1/t]

Subscripts

x,y	x and y direction (defined in Fig. 9)
i,j	x,y

Abbreviations

rpm	Revolutions per minute
DE, NDE	Drive end, non-drive end
TP	Tilting-pad
FPTP	Flexible-pivot tilting-pad

CHAPTER I

INTRODUCTION

Tilting-pad (TP) journal bearings are customarily used to support high speed rotating machinery such as centrifugal compressors and pumps, gas and steam turbines, among others. Fig. 1 depicts a schematic of a conventional TP bearing with four pads and the basic geometric characteristics.

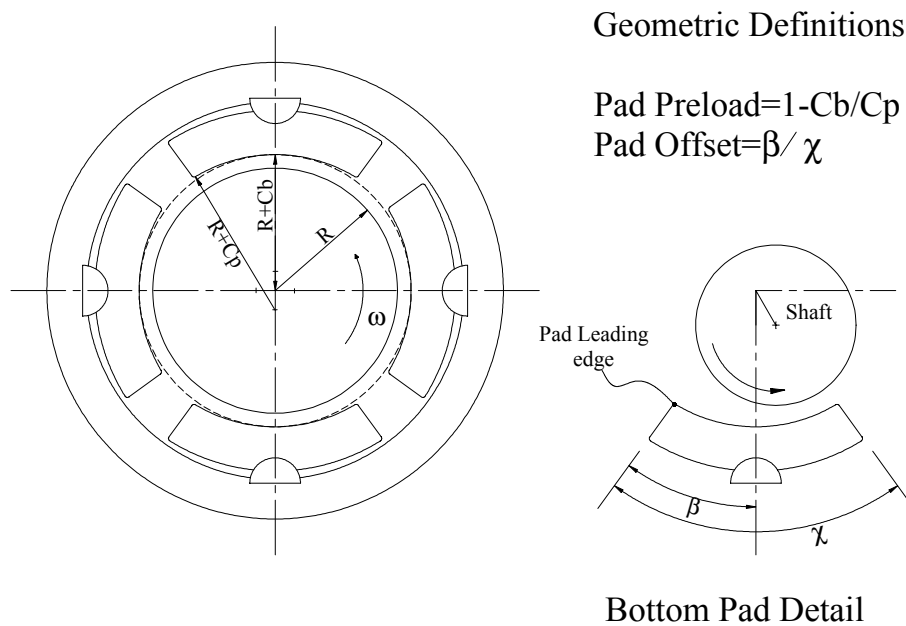


Fig. 1 Tilting pad bearing configuration

This thesis follows the style and format of the Journal of Engineering for Gas Turbines and Power.

TP bearings are characterized by the inherent stability that arises from their low cross coupling. A bearing is said to have cross coupling when the supported rotor moves *both* along and orthogonal to the direction of a given applied load. This characteristic is unique of rotating machines operating in fluid film bearings and it can cause self-excited vibrations and dynamic instabilities that often lead to machine failure and damage. The stabilizing feature of TP bearings makes them suitable as retrofits for unstable machines, as well as for new machines that require maximum rotordynamic stability [1].

TP bearings differ from fixed geometry journal bearings in that the pads are able to tilt freely about a pivot. The pivot configuration can be spherical, as illustrated in Fig. 1, rocker type, among others.

Flexible-pivot tilting-pad (FPTP) bearings achieve low cross coupling via flexural rotation of the pad's "web" support. The web is a beam element that provides enough radial stiffness to support bearing radial loads, and still permits the pads to tilt. Fig. 2 shows a schematic of a FPTP bearing with a detail of the web support.

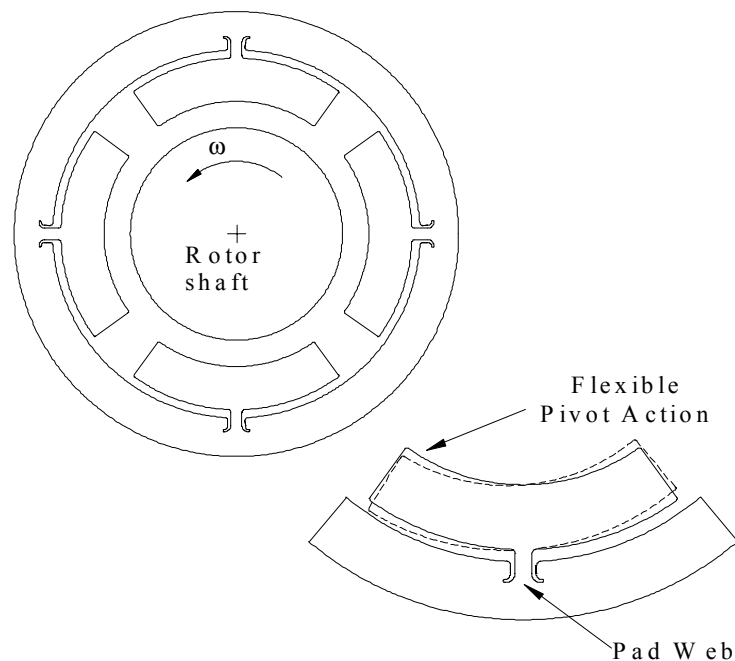


Fig. 2 Flexible-pivot tilting pad bearing

State-of-the-art electro-discharge machining process allows the manufacture of this single-piece while providing accurate control of geometric tolerances. This is a convenient design since it is a single-piece part as opposed to the TP bearing multi-piece design. TP bearings can be difficult to assemble and their pivot support can wear rapidly, which degrades bearing performance. FPTP bearings eliminate pad-pivot wear, since there are no parts in relative sliding motion (Zeidan and Paquette [1], and Armentrout and Paquette [2]).

Reliable rotordynamic calculations, namely critical speeds, response to imbalance, and instability margins must include the effect of bearing flexibility and damping [3]. Linear analysis relies on the representation of a journal bearing with linearized stiffness and damping coefficients. Fig. 3 shows a schematic side view of a rotor supported by a fluid film bearing with the linearized dynamic coefficients.

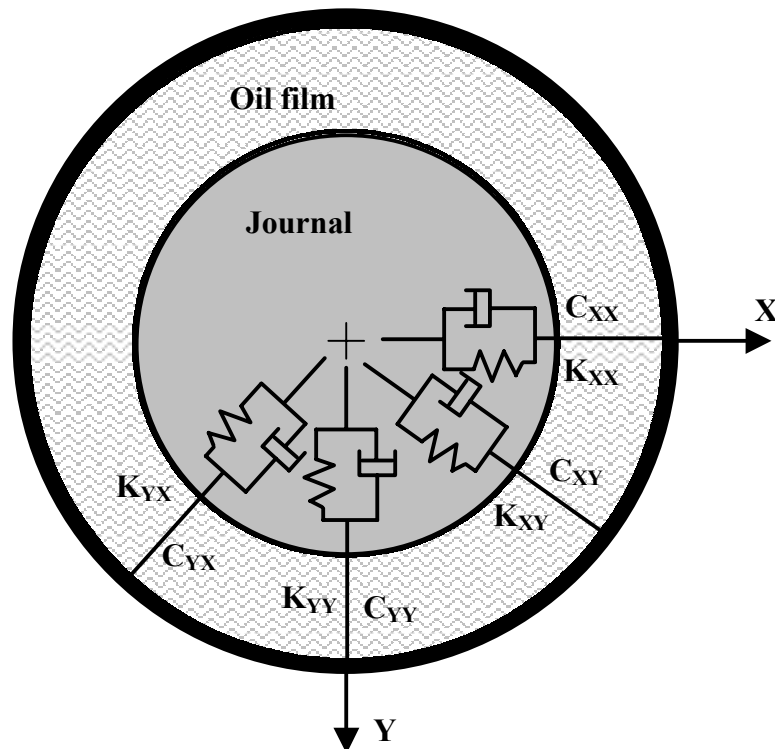


Fig. 3 Linearized bearing coefficients

The main rotordynamic issue concerning TP bearings is the theoretical prediction that the stiffness and damping coefficients are dependent upon the frequency of excitation (Barret et al. [4]). There are very limited experimental results in the public-domain literature to support this prediction. Understanding the nonsynchronous dynamic characteristics of these bearings is essential for sound rotordynamic modeling to accurately predict rotor critical speeds and stability of machines.

Rotordynamic coefficient results from this investigation show that the stiffness coefficients are strongly dependent upon the frequency of excitation. The source of the frequency dependency is twofold; first, the dynamics introduced by the pads' degrees of freedom and second, the effects of the inertial forces generated by the lubricant film. The combined effects can be accounted for with an added-mass coefficient matrix. This approach allows the description of the bearing force with three frequency-independent stiffness, damping and added-mass coefficient matrices.

Customarily, the effect of the fluid inertia is neglected when calculating the dynamic coefficients of journal bearings on the basis that the flow regime is mostly laminar. However, in 1975 Reinhardt and Lund [5] demonstrated that in some instances the added-mass coefficients could be significant even for a journal bearing operating in a laminar flow regime. The experimental results presented in this thesis are compared to predictions of an analysis and computer code by San Andres [6] that includes the solution of the bulk flow Navier-Stokes equations for TPDFP bearings including the effects of fluid inertia.

The test bearing is a four-pad tilting pad bearing with a load-on-pad configuration, i.e., the static load is oriented at the bottom pad's pivot. The bearing diameter is 116.8 mm, and the length is 76.2 mm (Length-to-diameter ratio is 0.65). The bearing radial clearance is 0.1905 mm, and the pad radial clearance is 0.254 mm. The test conditions include four shaft rotational speeds 6000, 9000, 13000 and 16000 rpm, and bearing static unit loads from 172 kPa to 689 kPa. Results also include steady-state performance measurements, including bearing static load versus deflection characteristics, pad metal temperatures, and estimated power losses.

CHAPTER II

LITERATURE REVIEW

Lund [3] presented the first method for calculating stiffness and damping coefficients for TP journal bearings. His approach is the so-called pad assembly method and consists of calculating the dynamic coefficients of a single rigid pad, using Reynolds equation, and finally adding the contribution of the loaded pads. Later, Nicholas et al. [4] modified this approach to include the effect of the unloaded pads and used finite elements instead of finite-differences to solve the hydrodynamic pressure field.

The pad's rotational degree of freedom requires additional dynamic coefficients to describe the translational dynamics of a rotor supported on TP bearings. Barret et al. [4] state that $2 \cdot (5 \cdot N_{PAD} + 4)$ dynamic coefficients are needed when analyzing the dynamics of a rotor mounted on TP bearings, as opposed to the case of fixed geometry bearing where only 8 are needed. For rotordynamic calculations, the common practice is to eliminate the pad degree of freedom by assuming a given frequency of pad rotation and derive eight "reduced" bearing dynamic coefficients equivalent to a fixed geometry bearing. A usual assumption is that the system is undergoing synchronous harmonic motion [3], such as imbalance response. However, should the system vibrate at frequencies other than the rotor running speed, the question is whether the reduced dynamic coefficients significantly change with vibration frequency. Barret et al. [4] showed that, for some bearing characteristics and operating conditions, there is little influence of the ratio of vibration frequency to shaft rotational speed on the reduced coefficients and therefore the synchronously reduced coefficients are fairly good for stability and critical speed calculations.

Most of the experimental results for rotordynamic coefficients of tilting pad bearings available in the public-domain literature are obtained by using synchronous excitation forces. However, Ha and Yang [8] measured stiffness and damping

coefficients varying the frequency of the excitation force for a 300.9 mm diameter, five-pad, tilting pad bearing. The aim was to determine whether the frequency of excitation affected the stiffness and damping coefficients of a TP bearing. The experiments included shaft speeds to 3,600 rpm and bearing loads to 220 kPa, and excitation frequencies ranging from 60% to 90% of the shaft synchronous frequency. The stiffness coefficients either decreased slightly or remained constant with frequency, and the damping increased slightly.

Chen [9] presented a pad assembly method to calculate *reduced* dynamic stiffness and damping coefficients for FPTP bearings using Reynolds equation, including the effects of the *radial* flexibility of the support web and the inertia of the pad. He concluded that the flexibility of the support web could lower the damping coefficients and also generate destabilizing cross-coupled stiffness coefficients.

Some form of the Reynolds equation (laminar or turbulent) is normally used to model TP and also FPTP bearings. A perturbation analysis for small motion about an equilibrium position produces perturbed reaction forces that define the rotordynamic coefficients. The Reynolds equation is a simplified form of the Navier-Stokes equations that neglects the temporal and convective acceleration terms of the momentum transport equations. The majority of the commercially available bearing computer codes for calculating dynamic coefficients rely on the Reynolds equation, and consequently neglect fluid inertia effects.

However, Reinhardt and Lund [5] argue that while this assumption is valid for Reynolds numbers smaller than 100, for larger Reynolds numbers, the inertia of the fluid may influence the bearing dynamic coefficients, even for laminar flow. They solved Reynolds equation without neglecting fluid inertia terms and calculated added-mass coefficients. They found that the added-mass coefficients for journal bearings could be significant and concluded that they could be important for certain applications, such as short light rotors.

San Andrés [10] presented a bulk flow model for hydrostatic bearings including the effects of variable fluid properties, turbulent flow, and fluid inertia. A perturbation of

the momentum and energy transport equations that govern the flow in the bearing fluid film is used to determine the bearing steady-state response and dynamic force coefficients. In this model, the temporal and convective acceleration terms are included in the momentum transport equations.

Franchek et al. [11] presented experimental rotordynamic coefficients for a high-speed, high-pressure, orifice-compensated hybrid (combination of hydrostatic and hydrodynamic) bearing and compared the results with predictions with San Andrés' bulk flow model. Good agreement was obtained between theory and experiment for stiffness and damping coefficients. For the added-mass coefficients the agreement was only fair. However, the magnitudes were comparable.

San Andrés later extended his model for TP and FPTP bearings. He presented the application of this model/computer code to a high-speed hybrid FPTP bearing [6]. His numerical predictions agree very well with other theoretical calculations by Chen [9] for FPTP bearings operating under laminar flow conditions.

The static (or steady-state) performance characteristics of a bearing include load capacity (load/deflection curve), required oil flow rate, temperature rise between oil inlet and outlet, pad metal temperatures and power losses. There is a wealth of experimental and theoretical results in the technical literature concerning the steady-state performance of tilting pad journal bearings.

Pettinato and De Choudhury [12] presented test results of performance measurements for two types of five-shoe TP bearings. Data include pad metal temperatures, power loss and operating equilibrium position. The pads were instrumented with embedded thermocouples placed at several circumferential locations to show the temperature variation from the leading to trailing edge. Power losses were estimated by the difference between inlet and outlet oil temperature, and were found to be more speed dependent than load dependent. Measurements of journal equilibrium position confirmed the observation by other researchers that the journal also moves in the direction *orthogonal* to the static load, rather than exclusively moving along the direction of the force, confirming the presence of cross-coupling forces for TP bearings.

De Choudhury et al. [13] detailed performance measurements in a FPTP bearing for a high-speed centrifugal compressor. When compared to a conventional TP bearing, the FPTP bearing was found to operate at lower exit oil temperatures and cause less power loss, while maintaining the required stability characteristics.

San Andrés and Jackson [14] measured bearing displacement and pad leading and trailing edge temperatures for a four-pad flexible pivot tilting-pad bearing, and results were compared to theoretical predictions with good correlation. The bearing did not show any subsynchronous unstable vibrations, though cross-coupling due to the web flexural stiffness was observable in the static equilibrium position results.

CHAPTER III

DESCRIPTION OF THE TEST RIG

OVERVIEW

Fig. 4 depicts the test rig used to measure the static and dynamic performance of high-speed TP journal bearings. Kaul [15] presents a detailed account of the design and features of the test rig and facility at the Texas A&M Turbomachinery Laboratory. A summary of its main features follows.

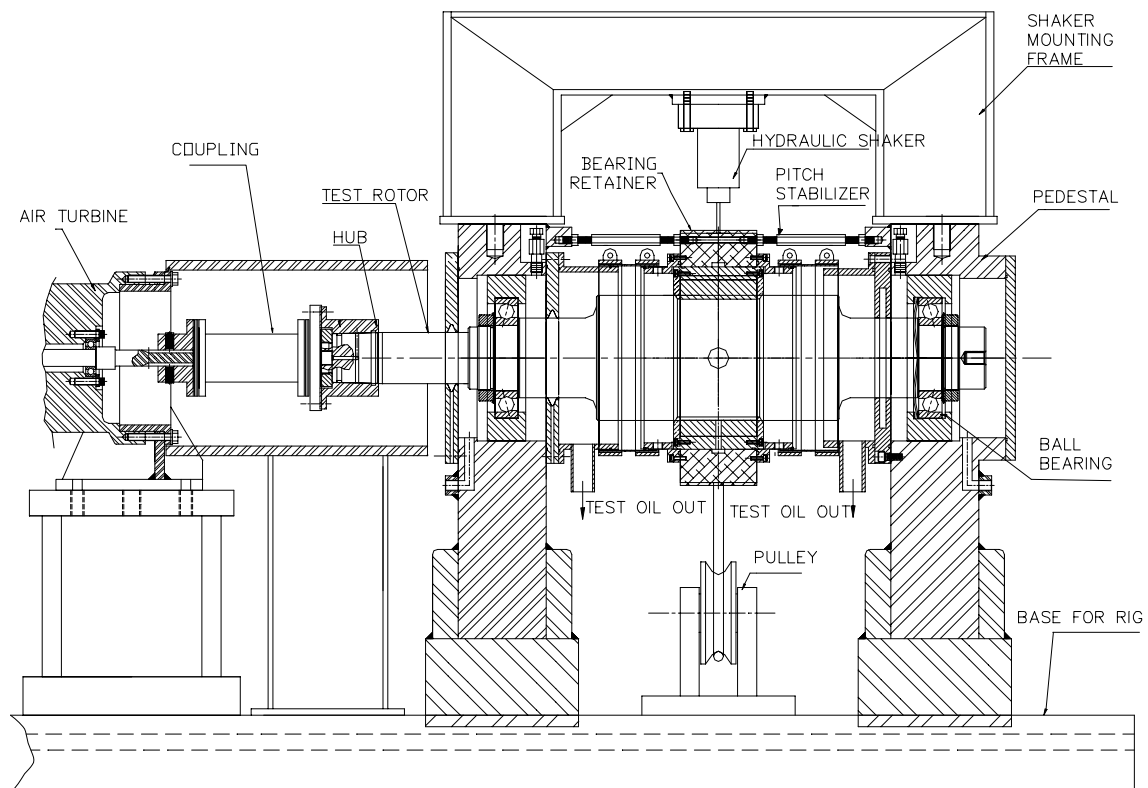


Fig. 4 Test rig main test section

The rig consists of a steel base that supports the main test section and the air turbine that drives the shaft. The shaft is connected to a 65 kW-power air turbine with a high-speed flexible disc coupling and can run up to a maximum speed of 17,000 rpm. The test shaft is made from stainless steel and machined to a precise diameter of 116.8095 mm at the test section. It is supported on the pedestals through angular contact ball bearings, spaced approximately 457 mm apart. An oil-mist lubrication system is used for lubricating the ball bearings.

A stator section holds the test bearing and all the associated instrumentation, namely, non-contacting eddy-current proximity sensors, accelerometers, pressure transducers and thermocouples. A pneumatic loader and two hydraulic shakers apply static and dynamic loads to the bearing stator. Angular alignment between the bearing and the shaft is provided by an arrangement of six pitch stabilizers.

ISO VG32 turbine oil is delivered to the test section from an oil supply system. The oil supply system can deliver oil up to a maximum pressure of 82.7 bars and a volumetric flow of 75 liters per minute. A heat exchanger and a set of pneumatically driven valves allow for control of the temperature of the oil being delivered to the test section.

LOADING CONFIGURATION

Two orthogonally mounted hydraulic shaker heads are attached to the stator middle section. The stator-shaker-stinger arrangement is shown in Fig. 5, as observed from the non-drive end. The shaker in the x -direction can excite the stator with dynamic loads up to 4450 N in tension and compression, the shaker in the y -direction can excite the stator with dynamic loads up to 4450 N in tension and 11125 N in compression. Both shakers can provide excitation frequencies up to 1000 Hz.

The shaker heads are attached to the stators through beam elements called stingers. Stingers isolate the test structure from the dynamics of the shakers structure. The load applied to the stator is measured with load cells bolted to the stingers on one end and the shaker head in the other end.

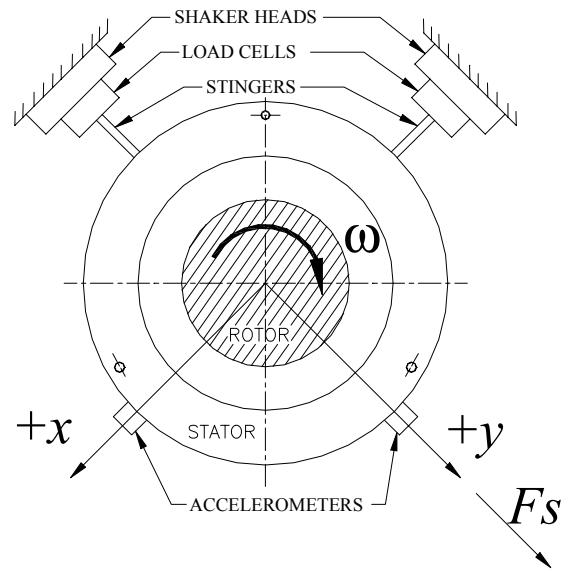


Fig. 5 Shaker-stinger configuration

While the shakers provide dynamic loads exclusively, the pneumatic loader applies a static tensile load to the stator in one direction. Fig. 6 shows the static loader assembly. The stator is displaced in the $+y$ direction due to the static load. A cable is connected to the stator assembly through a pulley and a yoke, and a spring system assures that the load is applied exclusively in one direction. The applied load is measured with a load cell attached to the cable. The rated maximum available load is 22000 N.

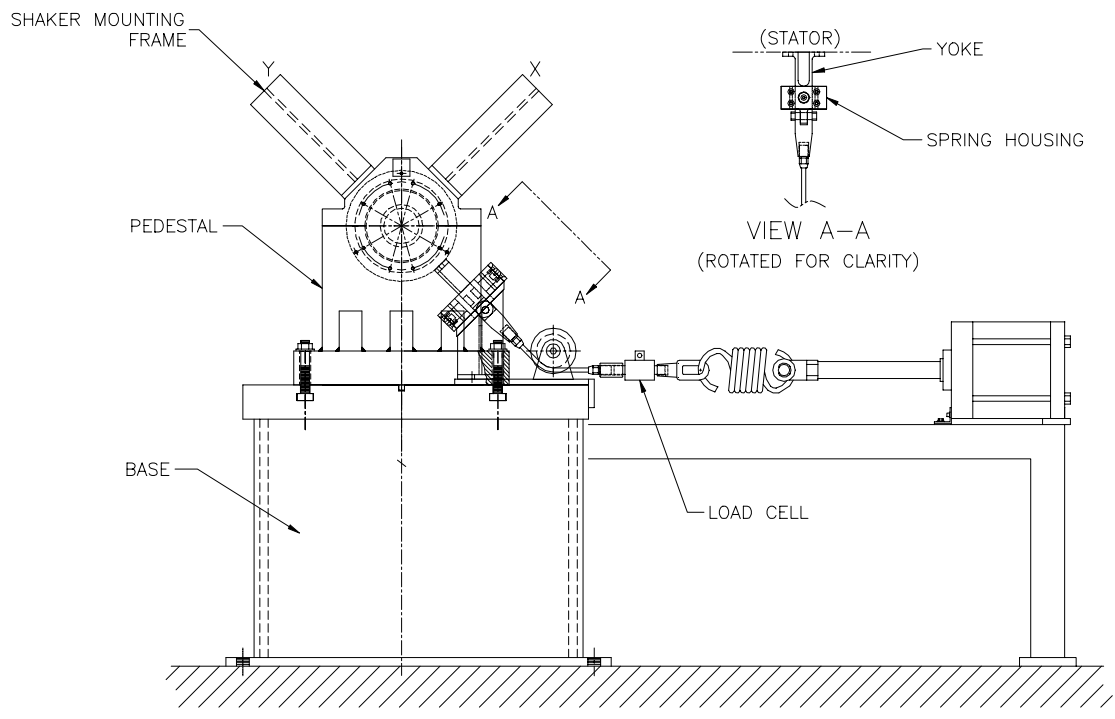


Fig. 6 Static loader assembly

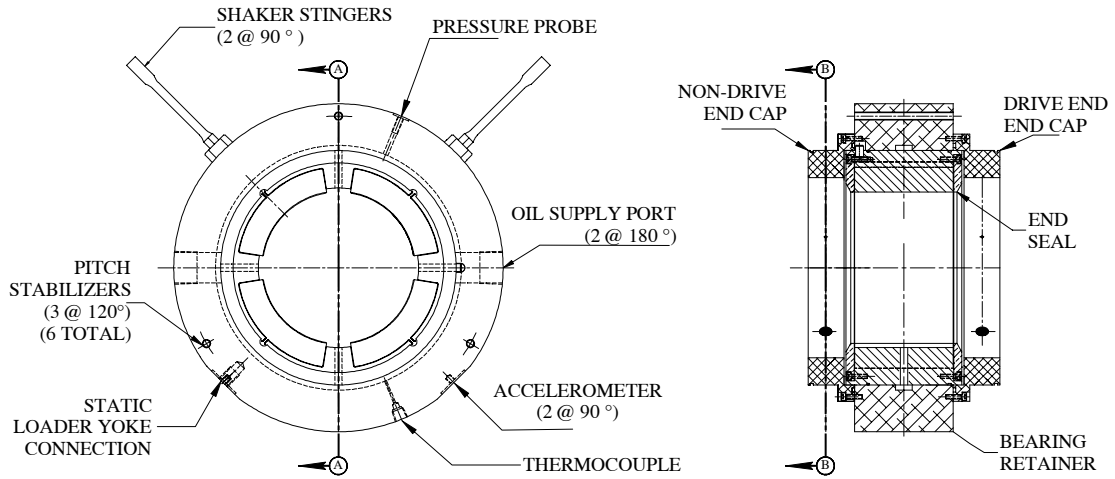
INSTRUMENTATION

Four proximity probes, located in the stator end caps record the relative motion of the stator with respect to the rotor for each direction of excitation. Two proximity probes are placed in a plane at the non-drive end and two at a parallel plane at the drive end. Measurement of the stator position in two parallel planes allow monitoring of the stator's pitch and yaw.

Piezoelectric accelerometers measure the stator absolute acceleration in both the x and y directions. Temperature probes are located in the oil-inlet chamber as well as the downstream end caps. A static pressure probe measures the oil pressure in the inlet channel and a conventional bourbon-type pressure gauge measures the oil outlet pressure, which is close to ambient, i.e., 0.1 bar.

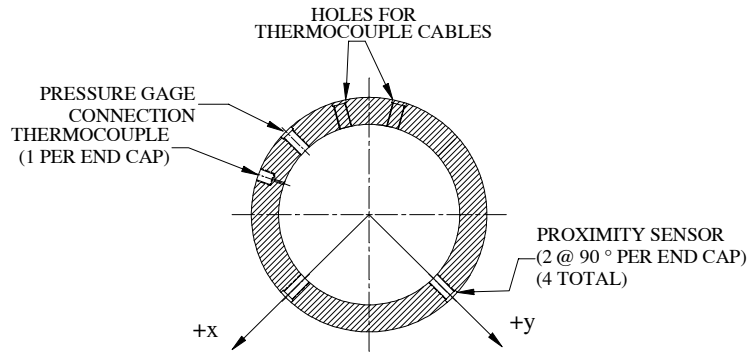
Fig. 7 shows the stator assembly, which is comprised of the test bearing and end seals, the retainer and the end caps. The oil is supplied to the bearing through two opposite entry ports placed in the retainer. The oil then flows through a circumferential groove between the retainer and the bearing outer diameter. Radial holes direct the oil to the space between the bearing pads. Seals located at each side of the bearing keep the oil from exiting freely in the axial direction. This configuration is often referred to as “flooded” lubrication.

The figure also details the location of all the measurement probes in the end caps and the retainer, as well as the location of the measurement planes.



STATOR - VIEW WITH END SEALS AND CAPS REMOVED

SECTION A-A: STATOR SECTION

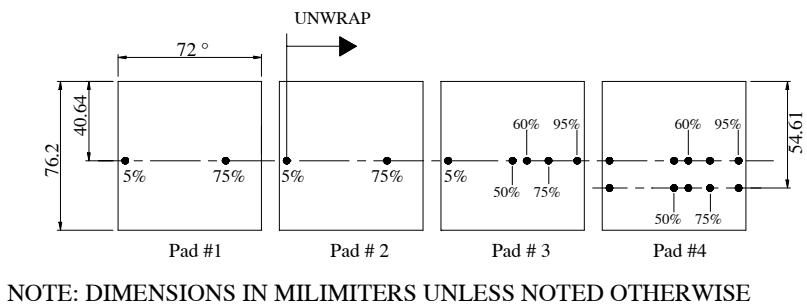
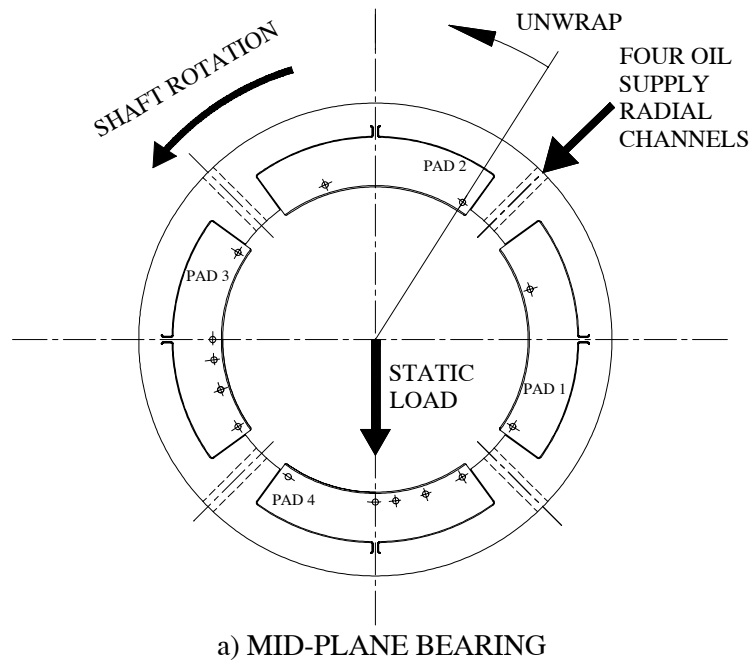


SECTION B-B: END CAP AS SEEN FROM THE NON-DRIVE END

Fig. 7 Bearing stator configuration and instrumentation

BEARING CHARACTERISTICS

Fig. 8 shows the four-pad high-speed flexible-pivot tilting pad bearing.



b) UNWRAPPED BEARING

Fig. 8 Bearing and pad thermocouples location

Pad metal temperatures are measured in several circumferential locations with embedded K-type thermocouples, located 3.81mm deep beneath the pads' babbited surfaces. The thermocouples are labeled according to their location as measured from the pads' leading edge, e.g. 5% of the pad length measured from the leading edge.

Table 1 summarizes the geometric characteristics and operating conditions of the test bearing.

Table 1 Bearing characteristics and operating conditions

No. of pads and load configuration	4 - Load on pad
Pad arc angle, χ	72°
Pivot offset, β	0.5
Pad clearance, C_P (m)	2.54×10^{-4}
Bearing clearance, C_B (m)	1.905×10^{-4}
Bearing preload ($1-C_b/C_p$)	0.25
Bearing diameter (m)	0.11684
Pad length (m)	0.0762
Lubricant	ISO VG 32 Steam turbine oil
Oil flow (L/min)	37.85 - 60.57
Oil inlet temperature (°C)	37.8
Pad rotational stiffness (N.m)	1695
Pad inertia (kg.m^2)	7.446×10^{-5}
Operating speeds (rpm)	6000 - 16000
Reynolds numbers	300 - 1000
Bearing unit loads (kPa)	172 - 1034

CHAPTER IV

THEORETICAL BACKGROUND

PARAMETER IDENTIFICATION MODEL

This section details the rotordynamic parameter identification procedure and has been adapted from Childs and Hale [16] and Rouvas and Childs [17]. The equations of motion for the stator mass M_s can be written as:

$$M_s \begin{bmatrix} \ddot{x}_s \\ \ddot{y}_s \end{bmatrix} = \begin{bmatrix} f_x \\ f_y \end{bmatrix} - \begin{bmatrix} f_{bx} \\ f_{by} \end{bmatrix} \quad (1)$$

where \ddot{x}_s, \ddot{y}_s are the *measured* components of the stator's acceleration, f_x, f_y are the *measured* excitation force, f_{bx}, f_{by} are the bearing reaction force components. The x and y subscripts in these equations identify the x and y direction, as depicted in Fig. 9.

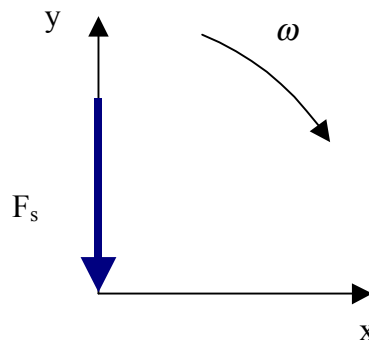


Fig. 9 Coordinate reference frame

The definition of the bearing reaction force as a function of the rotordynamic coefficients is given by:

$$-\begin{bmatrix} f_{bx} \\ f_{by} \end{bmatrix} = \begin{bmatrix} K_{xx} & K_{xy} \\ K_{yx} & K_{yy} \end{bmatrix} \begin{bmatrix} \Delta x \\ \Delta y \end{bmatrix} + \begin{bmatrix} C_{xx} & C_{xy} \\ C_{yx} & C_{yy} \end{bmatrix} \begin{bmatrix} \Delta \dot{x} \\ \Delta \dot{y} \end{bmatrix} + \begin{bmatrix} M_{xx} & M_{xy} \\ M_{yx} & M_{yy} \end{bmatrix} \begin{bmatrix} \Delta \ddot{x} \\ \Delta \ddot{y} \end{bmatrix} \quad (2)$$

Here $\Delta x, \Delta y$ are defined as the relative motion between the rotor and the stator and K_{ij}, C_{ij}, M_{ij} are matrices elements referring to stiffness, damping and added-mass coefficients, respectively.

Substituting Eq. 1 in Eq. 2 and rearranging, we obtain:

$$\begin{bmatrix} f_x - M_s \ddot{x}_s \\ f_y - M_s \ddot{y}_s \end{bmatrix} = - \begin{bmatrix} K_{xx} & K_{xy} \\ K_{yx} & K_{yy} \end{bmatrix} \begin{bmatrix} \Delta x \\ \Delta y \end{bmatrix} - \begin{bmatrix} C_{xx} & C_{xy} \\ C_{yx} & C_{yy} \end{bmatrix} \begin{bmatrix} \Delta \dot{x} \\ \Delta \dot{y} \end{bmatrix} - \begin{bmatrix} M_{xx} & M_{xy} \\ M_{yx} & M_{yy} \end{bmatrix} \begin{bmatrix} \Delta \ddot{x} \\ \Delta \ddot{y} \end{bmatrix} \quad (3)$$

The left hand vector of Eq. 3 is a known function of time. On the right hand side, $\Delta x(t)$ and $\Delta y(t)$ are measured functions of time. The rotordynamic coefficients are determined in the frequency domain via the Fast Fourier Transform version of Eq. 3, as shown below.

$$\begin{bmatrix} F_x - M_s A_x \\ F_y - M_s A_y \end{bmatrix} = - \begin{bmatrix} H_{xx} & H_{xy} \\ H_{yx} & H_{yy} \end{bmatrix} \begin{bmatrix} D_x \\ D_y \end{bmatrix} \quad (4)$$

The elements of the bearing dynamic stiffness function \mathbf{H} are related to the coefficients defined in Eq. 3 by:

$$\begin{aligned} H_{ij} &= (K_{ij} - \Omega^2 M_{ij}) + j(\Omega C_{ij}), \\ \text{Re}(H_{ij}) &= K_{ij} - \Omega^2 M_{ij}, \text{ and } \text{Im}(H_{ij}) = \Omega C_{ij} \end{aligned} \quad (5)$$

Eq. 4 provides only two equations for four unknowns \mathbf{H}_{xx} , \mathbf{H}_{xy} , \mathbf{H}_{yx} , \mathbf{H}_{yy} . To provide four independent equations, alternate shakes about a given steady-state rotor position are conducted on the stator in orthogonal directions (x and y) yielding four equations and four unknowns, given by:

$$\begin{bmatrix} F_{xx} - M_s A_{xx} & F_{xy} - M_s A_{xy} \\ F_{yx} - M_s A_{yx} & F_{yy} - M_s A_{yy} \end{bmatrix} = - \begin{bmatrix} H_{xx} & H_{xy} \\ H_{yx} & H_{yy} \end{bmatrix} \begin{bmatrix} D_{xx} & D_{xy} \\ D_{yx} & D_{yy} \end{bmatrix} \quad (6)$$

One set of frequency-dependent dynamic stiffnesses (\mathbf{H}_{xx} , \mathbf{H}_{xy} , \mathbf{H}_{yx} , \mathbf{H}_{yy}) is obtained as the average of 32 separate shake tests, which are averaged in the frequency domain. For most experimental conditions, ten consecutive tests are conducted to estimate the variability of the dynamic stiffnesses. In such cases, a total of 320 dynamic stiffness coefficients are measured for each frequency in the range of interest (i.e. 20-320 Hz).

The uncertainties of the dynamic stiffness are calculated, at each frequency, as *two* times the standard deviation of the ten individual dynamic stiffnesses obtained from each consecutive test. Uncertainties in the dynamic stiffness coefficients vary with frequency. Data at the frequency of 60 Hz, and its multiples, are contaminated by electrical noise and are consistently poor. These values substantially deviate from the rest of the data and are dropped. Similarly, data near or at the shaft's rotation synchronous frequency is also scattered with large uncertainties and are also eliminated.

CURVE-FITTING PROCEDURE AND UNCERTAINTY ANALYSIS

Eq. 5 shows that the real part of the dynamic stiffness is a quadratic function of the excitation frequency, whereas the imaginary part is a linear function. However, setting $\Lambda = \Omega^2$ transforms the quadratic into a linear relationship, thus a simple linear regression can be performed for both the real and the imaginary parts.

The intercept and the slope of the regression line of the real part provide *estimates* for the bearing stiffness (K_{ij}) and added-mass (M_{ij}) coefficients, respectively.

Similarly, the *estimates* for the damping coefficients (C_{ij}) are obtained from the slope of the linear regression of the imaginary part of the dynamic stiffness. Note that the intercept lacks physical meaning in this case, as suggested by Eq. 5, and therefore are not reported.

Here, “estimates” is a statistical term introduced for the following reasons: (i) the rotordynamic coefficients are not directly measured but rather are extracted from the experimental dynamic stiffness data, and (ii) only limited amounts of data are obtained, which introduces sampling error. Other additional sources of error are the measurement uncertainty of the instrumentation and the fact that the data do not present perfect parabolas or lines.

Confidence intervals are used to provide the uncertainty of the estimated rotordynamic coefficients considering the above factors. A confidence interval is a statistical measure of the error bound for the estimate of the slope (or the intercept), to assess the overall quality of the regression line and thus the accuracy of the estimates.

The formulas to compute the slope, the intercept and their associated uncertainties are listed below¹. Here, the letters x and y refer to a pair of data (x_i, y_j) for the linear regression. They do not refer to the x and y directions as defined in Fig. 9.

Number of data pairs, (x_i, y_i) N

Regression line equation $\hat{y} = \beta_0 + \beta_1 x$; \hat{y} denotes the predicted value

Mean of the x 's $\bar{x} = \frac{1}{N} \sum_{i=1}^N x_i$

Mean of the y 's $\bar{y} = \frac{1}{N} \sum_{i=1}^N y_i$

¹ A complete analysis on linear regression and confidence intervals can be found in most reference books on statistical analysis, e.g. chapter 11 of Reference [18].

$$\text{Slope} \quad \beta_1 = \frac{\sum_{i=1}^N y_i x_i - N(\bar{y})(\bar{x})}{\sum_{i=1}^N x_i^2 - N(\bar{x})^2} \quad (7a)$$

$$\text{Intercept} \quad \beta_0 = \bar{y} - \beta_1 \bar{x} \quad (7b)$$

$$\text{Mean Square Error, } \hat{\sigma}^2 \quad \frac{\sum_{i=1}^N (y_i - \hat{y}_i)^2}{N - 2}$$

$$S_{xx} \quad \sum_{i=1}^N x_i^2 - N \bar{x}^2$$

$$\text{Uncertainty of the slope, } \Delta\beta_1 \quad t \times \sqrt{\frac{\hat{\sigma}^2}{S_{xx}}} \quad (7c)$$

$$\text{Uncertainty of the intercept, } \Delta\beta_0 \quad t \times \sqrt{\hat{\sigma}^2 \left(\frac{1}{N} + \frac{\bar{x}^2}{S_{xx}} \right)} \quad (7d)$$

Notice that the uncertainty includes a parameter denoted as t . In general terms, this is a multiplicative factor that depends on the desired probability that the unknown “true” parameter is contained in the interval $\beta_0 \pm \Delta\beta_0$ (or, $\beta_1 \pm \Delta\beta_1$). Obviously, a high probability is desirable, thus it is set to 95%, which yields $t=1.960$. This probability is commonly referred to as “confidence level”.

CHAPTER V

EXPERIMENTAL PROCEDURE

Static and dynamic data are taken in the conditions shown in Table 2. During a typical test, the shaft is brought up to the steady state conditions of rotational speed and oil inlet temperature, for a given static load. Bearing static equilibrium position, oil inlet and outlet temperatures, pad temperatures, static load and bearing oil flow rate data are taken several separate times at each steady-state condition and then averaged.

Table 2 Test conditions

ω [rpm]	\dot{Q} [LPM]	T_{in} [°C]	P [kPa]								
			172	259	345	431	517	603	690	862	1034
6000	37.854	37.8	X	O	X	O	X	O	X	O	
9000	37.854	37.8	X	O	X	O	X	O	X	O	O
13000	37.854	37.8	X	O	X	O	X	O	X	O	O
16000	60.567	39.4	X	O	X	O	X	O	X		

NOTES:

- 1 - Ten dynamic tests were done for the conditions marked with a 'X'
- 2 - Only steady-state data were recorded for the conditions marked with an 'O'

The bearing stator is then alternately excited using the hydraulic shakers with a pre-specified pseudo-random dynamic excitation in two orthogonal directions, i.e. x -direction and the y -direction (static load direction). Dynamic data include the bearing relative motion with respect to the shaft at the drive and the non-drive end, load applied by the shakers and absolute acceleration of the bearing stator. The data are captured in time domain and later transformed to the frequency domain with the Fast Fourier Transform and reduced with the procedure described earlier.

MEASUREMENT OF “BASELINE” DYNAMIC STIFFNESS

The tests aim to measure rotordynamic coefficients of the test bearing. However, the measurement procedure also measures stiffness and damping introduced by the pitch stabilizers, hose connections, etc. To account for these additional elements, ‘base-line’ tests were conducted with ‘dry shakes’ at zero rotor speed and no oil supplied to the bearing. Fig. 10 to Fig. 12 show the direct and cross-coupled baseline dynamic stiffnesses.

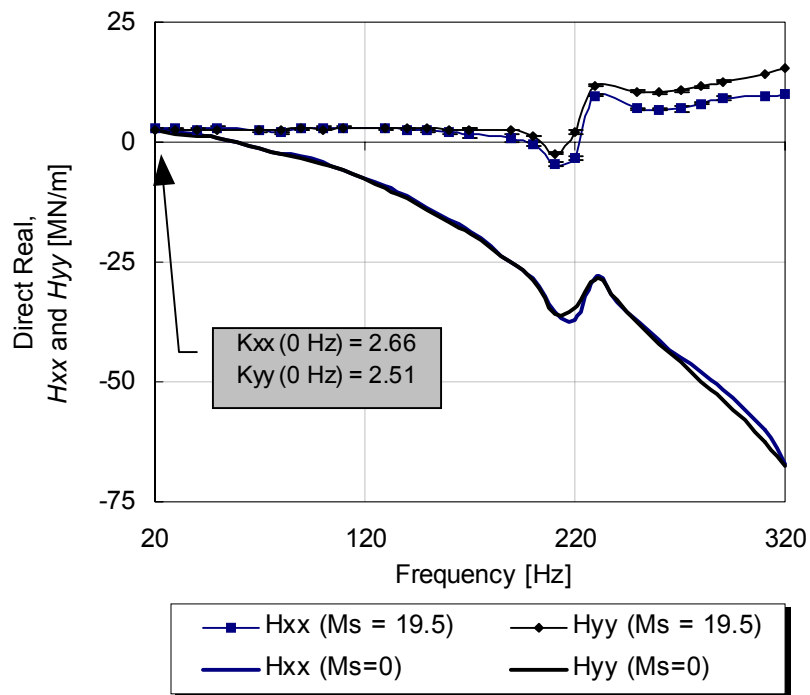


Fig. 10 Baseline real direct dynamic stiffness

Fig. 10 shows the real part of the direct baseline dynamic stiffness with and without subtracting the stator mass (M_s), as defined by Eq. 5. A curve-fit of the data of the solid curve for a frequency range from 20 to 100 Hz, yields a stator mass of approximately 19.5 kg, which agrees with the static measurement of the weight of the stator (18.9 kg).

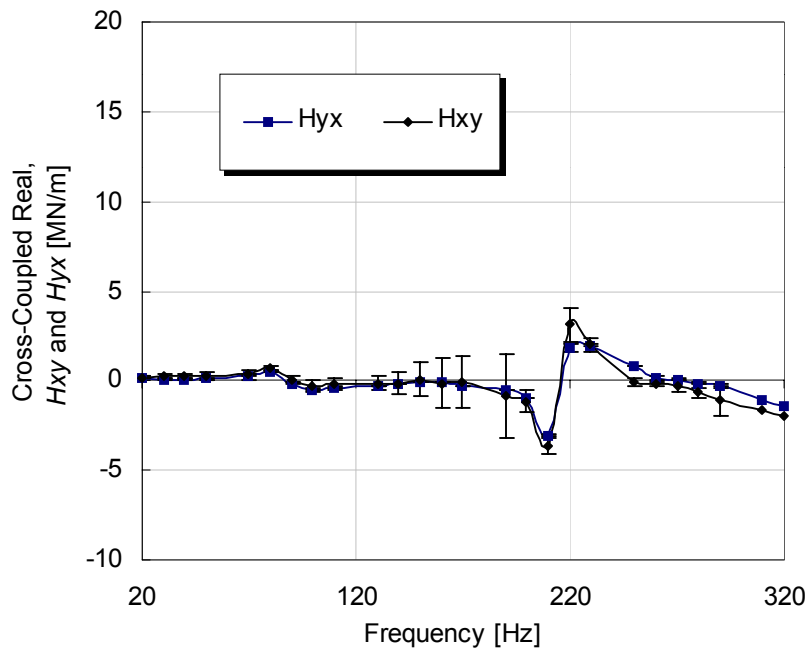


Fig. 11 Baseline real cross-coupled dynamic stiffness

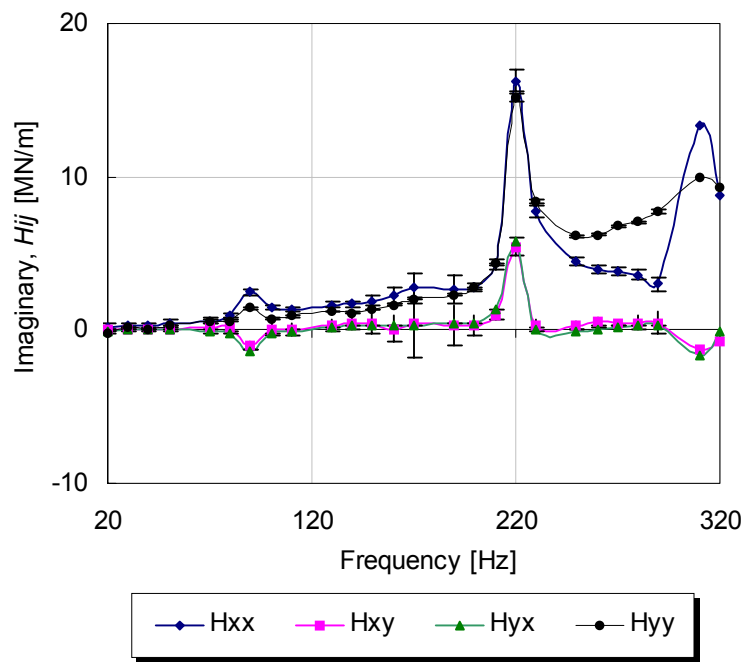


Fig. 12 Baseline imaginary dynamic stiffness

Fig. 13 shows the change in stator eccentricity as a result of static loads applied with the pneumatic loader. According to the relation $F_y = K_{yy} \cdot y$, the static (i.e. zero frequency) stiffness may be obtained as the slope of the force versus displacement curve. This yields a static stiffness of 2.69 MN/m in the direction of the load. The low-frequency stiffness obtained from the dry shake dynamic stiffness data is 2.51 MN/m (see Fig. 10), which agrees well with the static measurement.

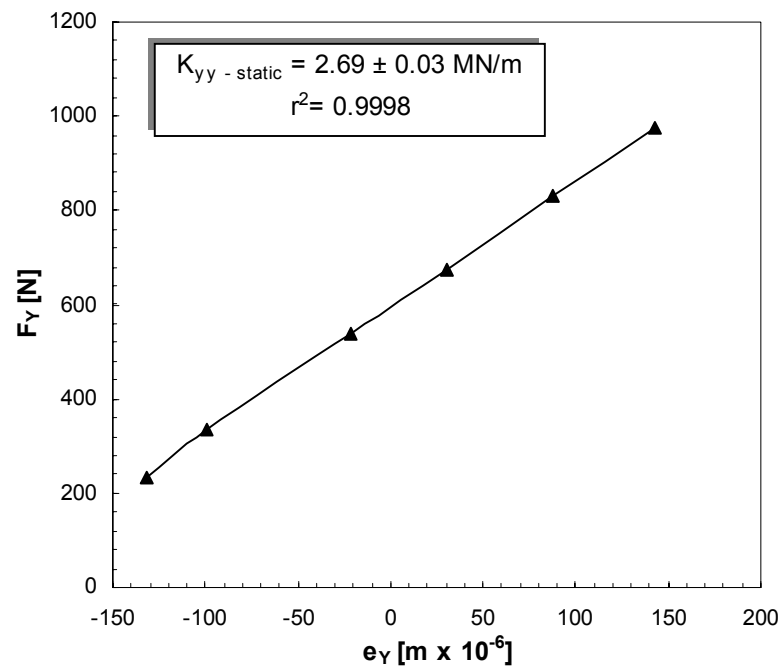


Fig. 13 Pitch stabilizers' static stiffness in the y-direction

CHAPTER VI

STATIC PERFORMANCE CHARACTERISTICS

This section includes the static (or steady-state) performance data. These include load capacity (load/deflection curve), pad metal temperatures and estimated power losses. There is a wealth of experimental and theoretical results in the technical literature concerning the steady-state performance of tilting pad journal bearings. In general, the results presented herein confirm these results.

The oil flow rate and inlet temperature were 37.38 liter per minute and 37 ± 2 °C, except for the largest shaft speed, 16000 rpm, for which the oil flow rate and inlet temperature were 60.57 liter per minute and 39.4 ± 2 °C. For this speed, the oil flow rate had to be increased to prevent excessive oil throw-off temperature.

The limiting factor for applying larger loads was the excessive proximity of the bearing to the shaft (to avoid rubbing). For the case of 16000 rpm, the limiting factor was the excessive temperature of the ball bearings, which reached their shut-off limit during testing.

Fig. 14 shows the bearing centerline loci as a function of the static load and rotational speed. Here the coordinates (e_x, e_y) are divided by the bearing pad clearance, C_p . The Figure shows that the bearing moves not only in the direction of the load, but also in the normal direction, due to bearing cross coupling.

In conventional TP bearings, the cross coupling is theoretically null (given the pads' mass moment of inertia are neglected). However, in the case of FPTP bearings, cross coupling is expected because the pads are not completely free to tilt as the structural web offers rotational stiffness, and also because of the mass moment inertia of the pads.

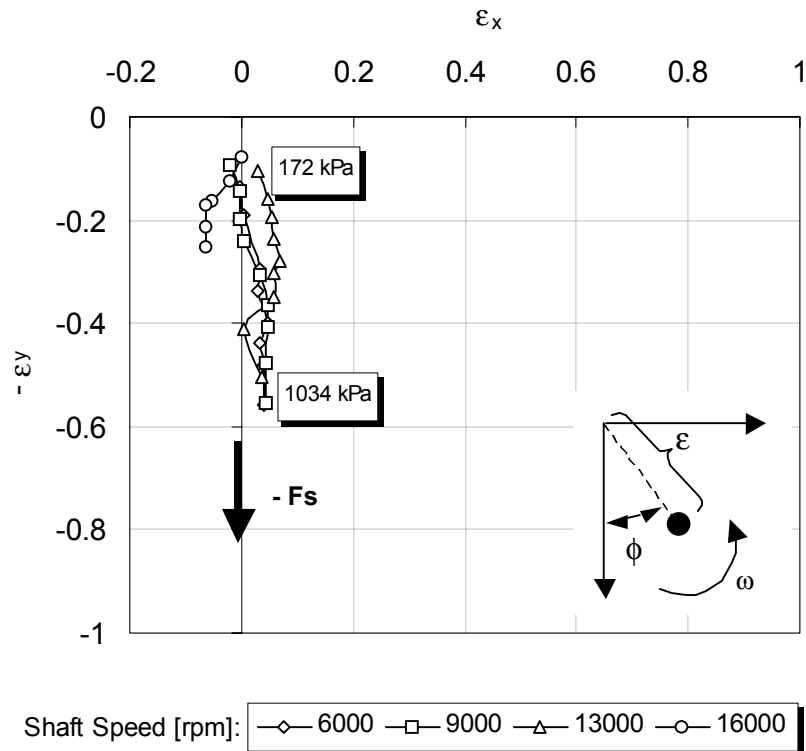


Fig. 14 Bearing centerline loci plots

The position of the bearing may be described with the eccentricity ratio ε and the attitude angle ϕ (see Fig. 14), as defined in the Equations below:

$$\varepsilon_x = \frac{e_x}{C_P}, \quad \varepsilon_y = \frac{e_y}{C_P}, \quad \varepsilon_{x0} = \frac{e_{x0}}{C_P}, \quad \varepsilon_{y0} = \frac{e_{y0}}{C_P}$$

$$\varepsilon = \sqrt{(\varepsilon_x - \varepsilon_{x0})^2 + (\varepsilon_y - \varepsilon_{y0})^2} \quad (8)$$

$$\phi = \operatorname{tg}^{-1} \left(\frac{\varepsilon_x - \varepsilon_{x0}}{\varepsilon_y - \varepsilon_{y0}} \right) \frac{180}{\pi} \quad [\text{deg}]$$

Fig. 15 shows the eccentricity ratio and Fig. 16 shows the attitude angle as a function of the bearing load.

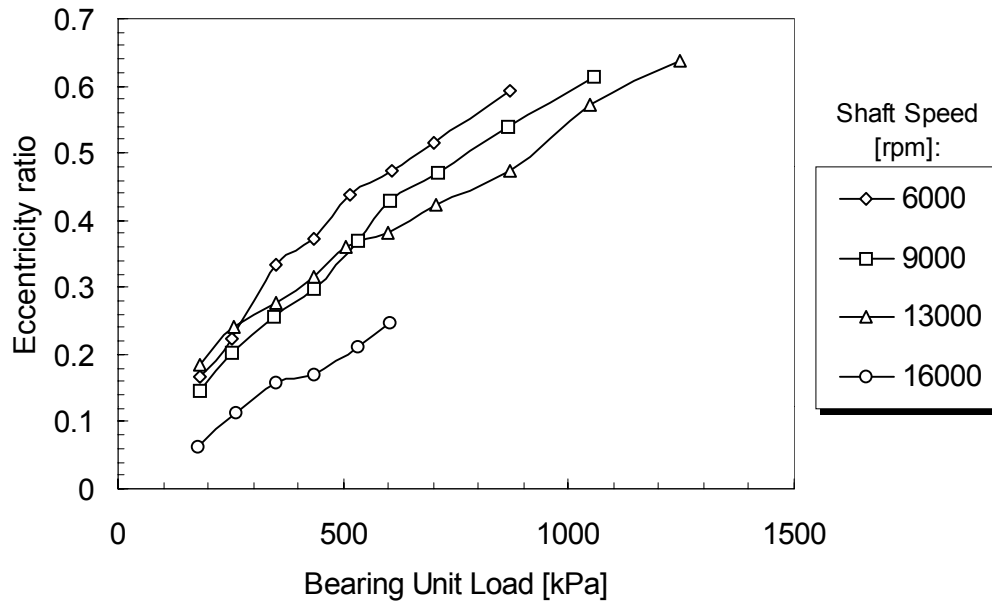


Fig. 15 Eccentricity ratio versus bearing unit load

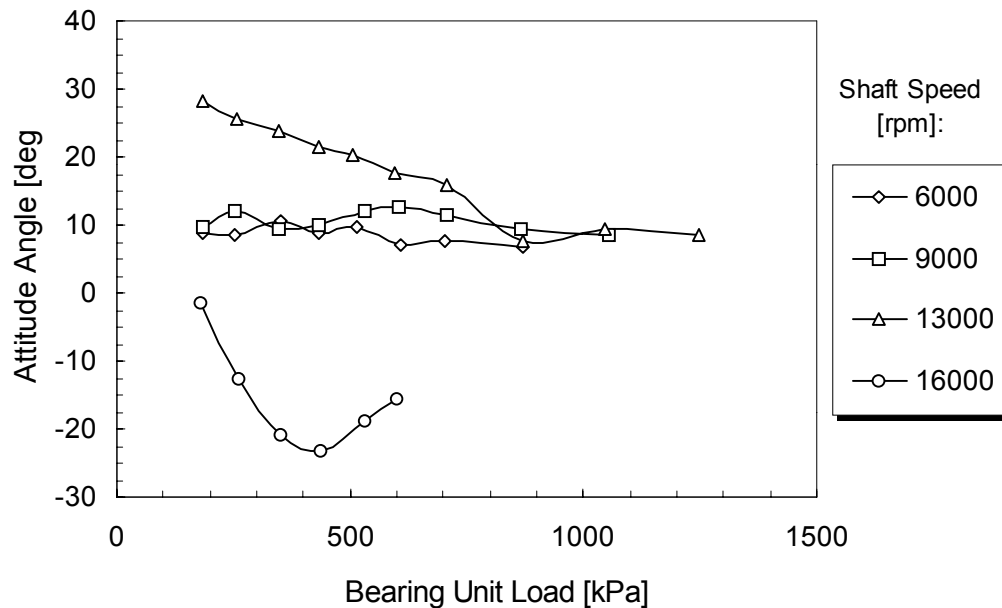


Fig. 16 Attitude angle versus bearing unit load

The attitude angle for 13000 rpm was larger than for the lower speeds. However, at a unit load of approximately 900 kPa, the bearing presented a sudden change in its static equilibrium position, moving closer to the vertical line, resulting in smaller attitude angles. For 16000, the bearing moved in the (-x) direction (negative attitude angle), even for small loads.

Fig. 17 depicts the temperature of the loaded pad at the 75% location, which is close to the trailing edge (refer to Fig. 8). Typically, the highest temperature in the bearings occurs at this location. The solid line represents the temperature at the centerline plane and the dashed line the temperature at the plane downstream. The difference between these two temperatures evidences some level of bearing to shaft misalignment.

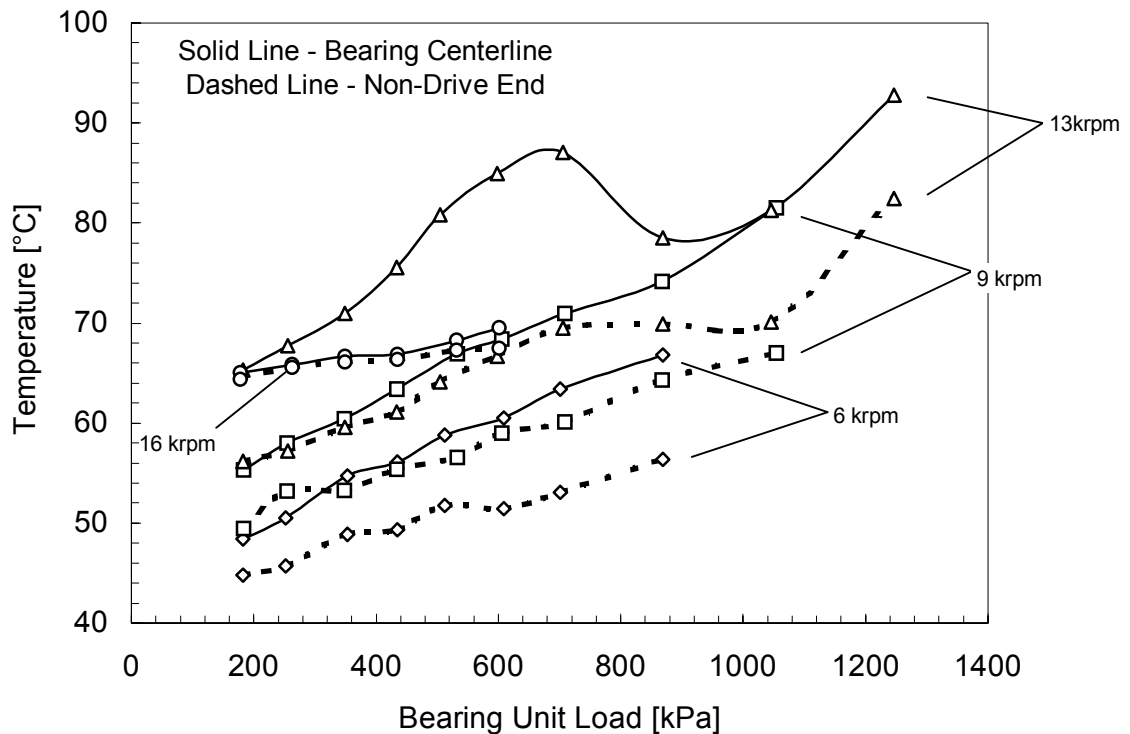


Fig. 17 Maximum temperature of the loaded pad

The trailing edge temperature increases almost linearly with load. Note that at a rotational speed of 13000 rpm and a load of 8000 N there is a sudden reduction in the maximum temperature, which is related to the “jump” in bearing position described earlier. Such sudden changes in the pad temperature are usually related to a change in the flow regime from laminar to turbulent, as observed by Bouchoule et al. [19]. Bearing to shaft misalignment might also play a role in the “jump” occurrence, as experience with preliminary tests revealed, where this behavior was repeatedly observed even at lower speeds until the bearing alignment was improved to the best of the test rig’s capabilities. However, a clear explanation of the physical principles behind this phenomenon is not available at the present moment.

At the largest speed, 16000 rpm, the maximum temperature was lower than for 13000 rpm. The temperature at this speed seems to be insensitive to bearing load and to

misalignment, as evidenced by the null axial temperature gradient. Note that the oil inlet temperature was slightly higher for this speed, as it could not be controlled to the same level as for the other speeds.

The bearing frictional power loss can be estimated from the change in the lubricant's bulk temperature, according to Eq. 8. Many investigators customarily use this simplified heat-balance approach (e.g. Pettinato and De Choudhury [12]).

$$\text{Power} = \rho \dot{Q} c_p (T_{in} - T_{out}) \quad (8)$$

A simple error-propagation calculation of Eq. 8 revealed that the uncertainty in the calculated power loss is approximately 4 kW, which is very high mainly due to the uncertainty in the temperature (1.2 °C). Fig. 18 shows the bearing frictional power loss as a function of the unit load and the rotational speed.

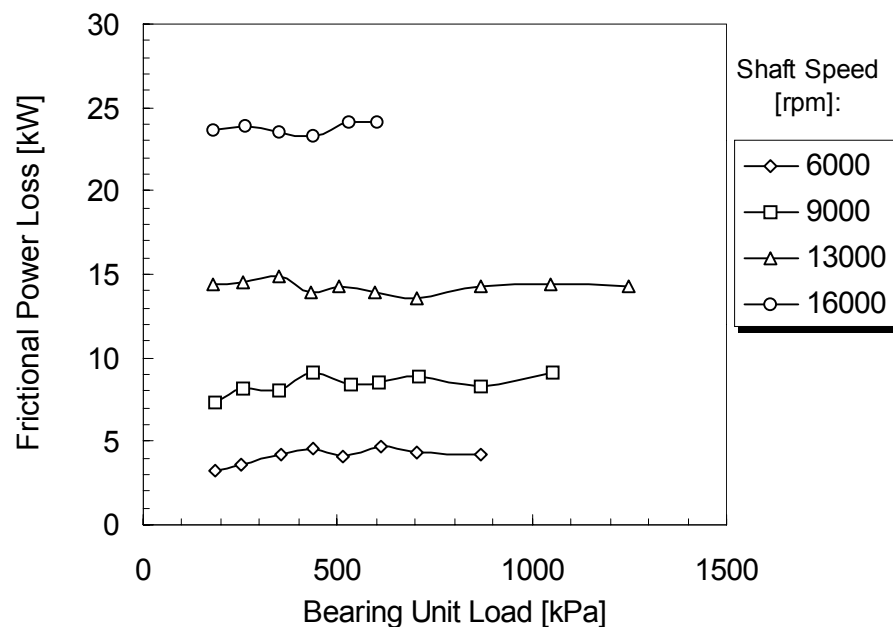


Fig. 18 Estimated frictional power loss

PAD TEMPERATURES

Fig. 19 and Fig. 20 show the pad temperature profiles for all rotational speeds tested and for four different bearing loads. Perhaps the obvious observation is that the temperature in the pad varies from the leading to the trailing edge. The highest values occur at the vicinity of the trailing edge of each pad. The pad with the highest temperatures is the loaded pad (#4), which is the pad that is closest to the shaft. Pad temperatures increase with shaft rotational speed.

Typically, the location of the highest temperature is not the location next to the trailing edge, as intuition would indicate (because of shear losses). Rather, the highest temperatures are found in the 75% location, because the fresh oil that is directed to the space between the pads cools the metal in the vicinity of trailing edge (95% location).

The measurements also confirm that hot oil is carried over from the trailing edge of one pad to the leading edge of the pad downstream. This is evidenced by the fact that the temperature of the leading edge of the pads is higher than the oil inlet temperature (37.85 °C).

Concerning the temperature profile for the rotational speed (16000 rpm), the temperatures of the unloaded pads are fairly similar to the temperatures of the loaded pad, which is not the case for the rest of the speeds. The temperatures of the unloaded pads at 16000 rpm are typically higher than for the rest of speeds.

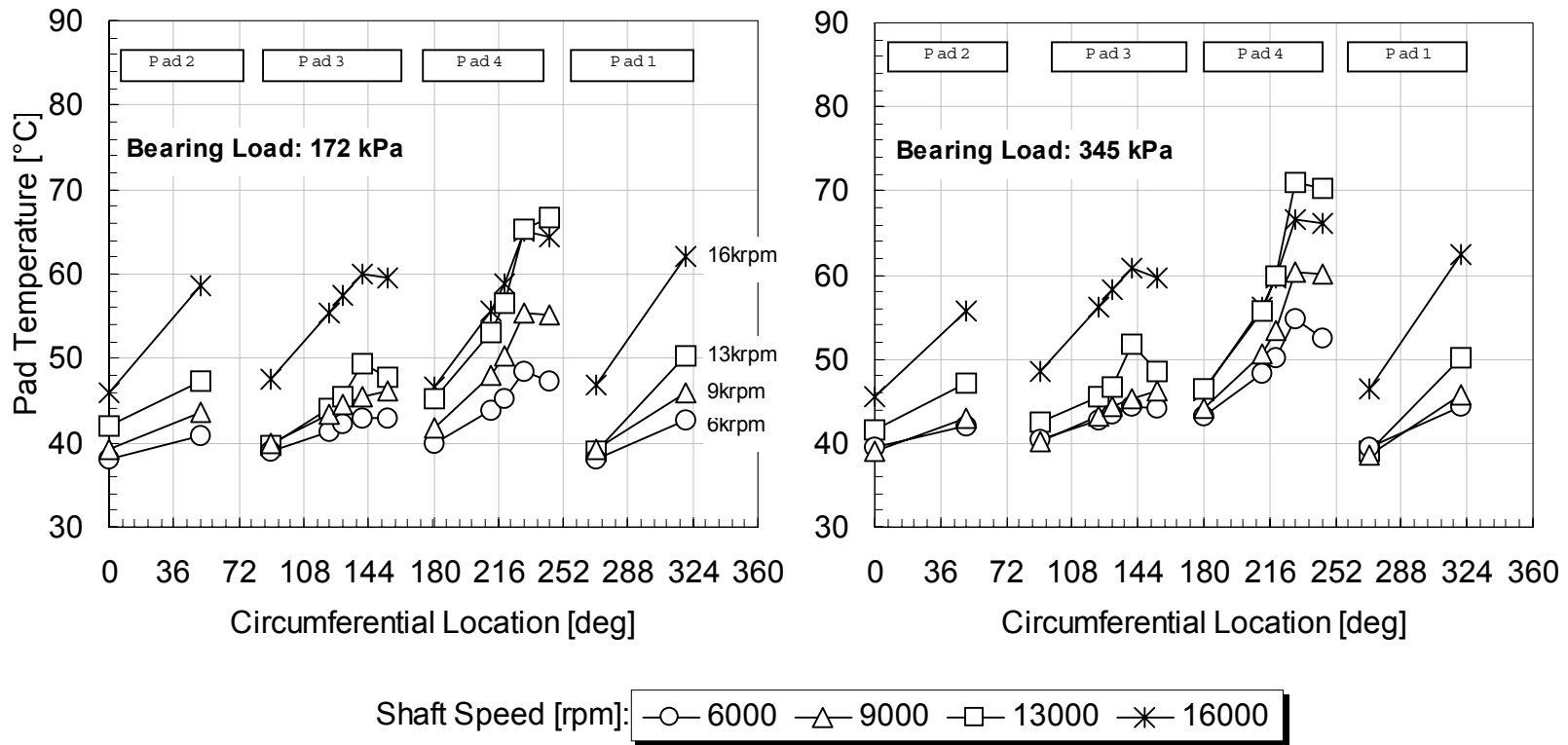


Fig. 19 Pad temperature profiles for 172 kPa (left) and 345 kPa (right)

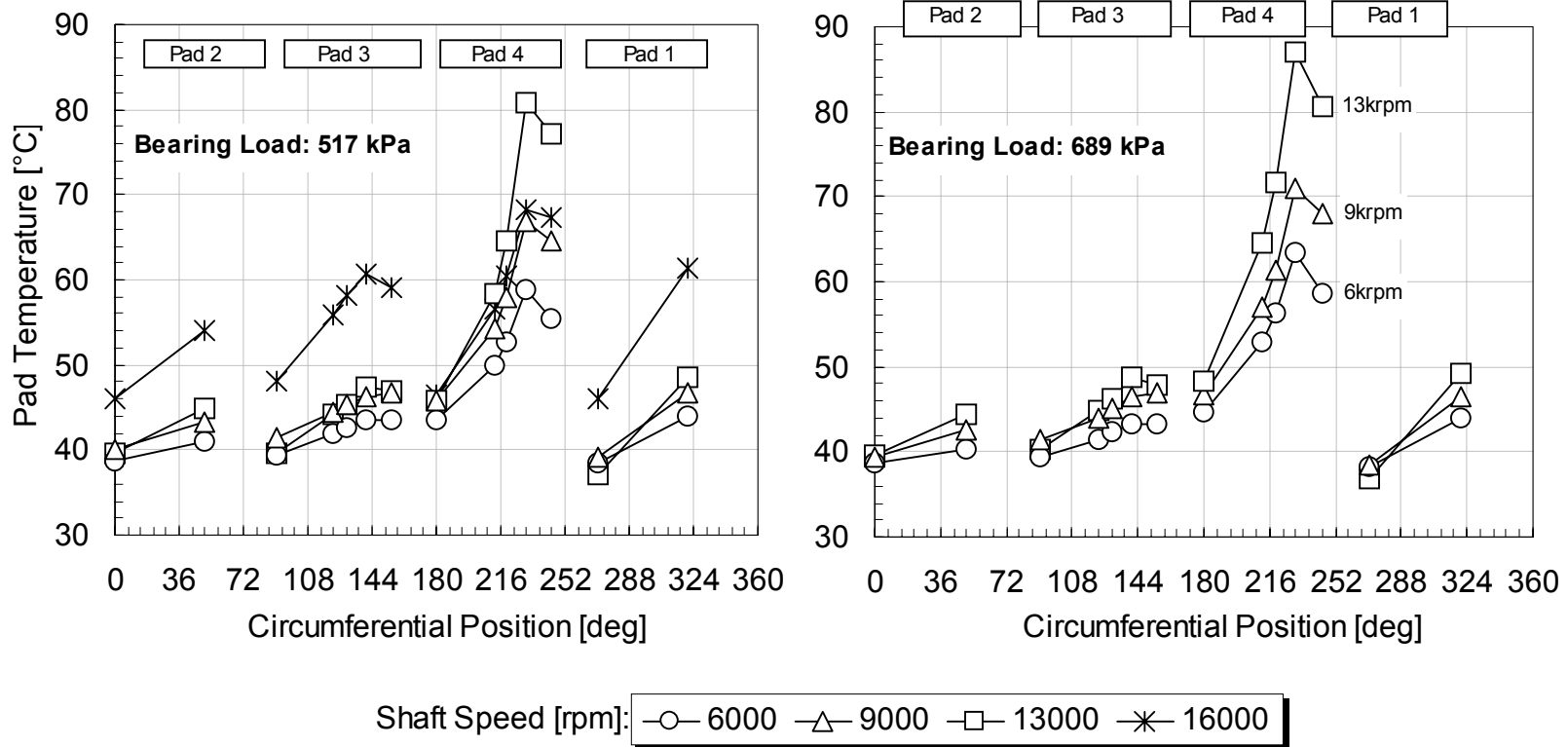


Fig. 20 Pad temperature profiles for 517 kPa (left) and 689 kPa (right)

CHAPTER VII

DYNAMIC STIFFNESS AND ROTORDYNAMIC COEFFICIENTS

BEARING DYNAMIC STIFFNESS

Fig. 21 to Fig. 24 show the real and imaginary parts of the dynamic stiffness for a rotor speed of 6000 rpm and a bearing unit load of 689 kPa. The baseline dynamic stiffnesses are included to show that they are fairly negligible compared to the actual measured values for the bearing. Uncertainty bars for the dynamic stiffnesses at each frequency indicate the degree of repeatability of the results during the ten consecutive tests performed to obtain the averaged dynamic stiffness coefficients.

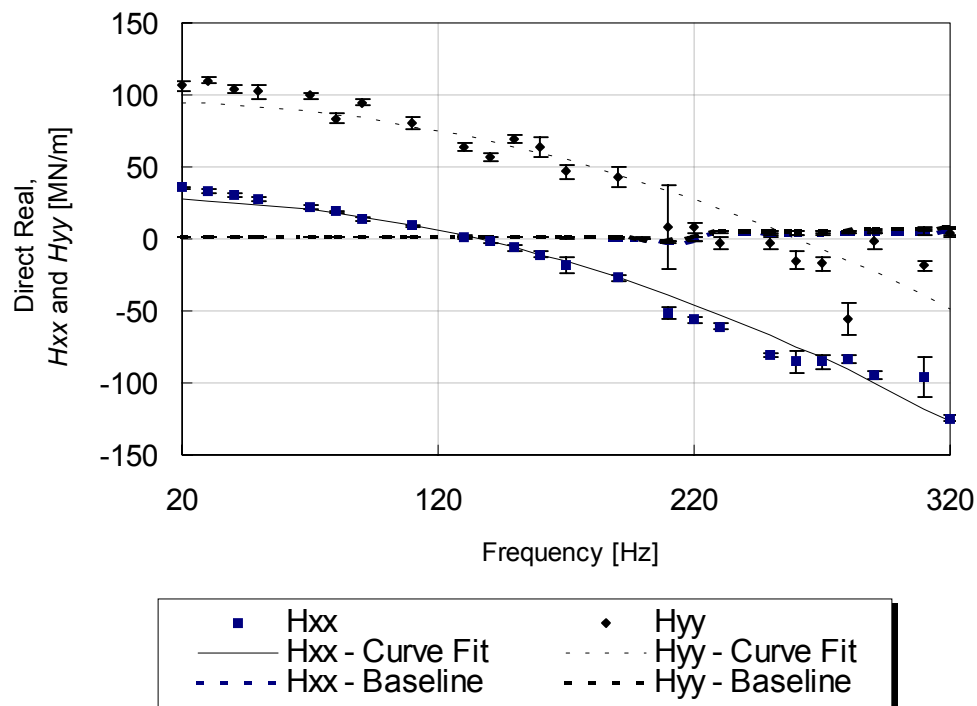


Fig. 21 Real direct dynamic stiffness at 6000 rpm and 689 kPa

Fig. 21 depicts the real part of the direct dynamic stiffnesses coefficients, H_{xx} and H_{yy} . Note that the dynamic stiffness decreases with increasing frequency until they actually become negative at certain frequencies. This behavior is due to the combined effects of the inertia of the fluid film and the frequency dependency due to the degrees of freedom of the pads.

The presence of added-mass coefficients in journal bearings due to fluid inertial forces is well documented by Reindhardt and Lund [4]. They argued that this would be the case even for bearings operating in a laminar regime, i.e., for Reynolds numbers with an order of magnitude of 10^2 . Representative Reynolds numbers corresponding to each actual test condition are shown in Table 3.

Table 3 Reynolds Numbers for Test Conditions

ω [rpm]	Re [-]
6000	300
9000	500
13000	800
16000	1000

Using their results, an approximate calculation for a journal bearing with comparable geometry to the bearing tested in this investigation yields an added-mass term of 10 kg. As discussed earlier, added-mass coefficients introduce a frequency dependency in the dynamic stiffness as shown by Eq. 9.

$$\text{Re}(H_{ij}) = K_{ij} - M_{ij} \Omega^2 \quad (9)$$

Additionally, the direct dynamic stiffness coefficients of a TP bearing should decrease with increasing frequency of vibration, as predicted by Barret et al.[4]. Actually, for a pad preload of 0.5, their numerical results show that coefficients decrease

25% to 30% when the vibration frequency is increased from almost zero to the synchronous frequency (i.e. the rotor's rotational frequency). Their numerical data includes a low Sommerfeld number ($S=0.2$), which signifies operation at a high load and/or at a low rotor speed, and $S=8$ (light load and/or high speeds).

Numerical data for a null pad preload show similar results for a low Sommerfeld number, whereas for $S=8$, the dynamic stiffness is reduced by as much as two order of magnitudes for the same frequency range. However, the range of Sommerfeld numbers of the tests results of the present investigation is approximately from 0.2 to 1.5. In conclusion, the results of Fig. 21 show that the dynamic stiffness is affected by the frequency dependency due to the pad degree of freedom and the effect of the inertia of the fluid. Incidentally, it follows from the preceding discussion that the frequency dependency is determined by both the bearing geometric characteristics and the operating conditions.

Ha and Yang [8] provide experimental stiffness and damping coefficients for a 300.9 mm-diameter and 149.8 mm-long TP bearing as a function of the frequency of excitation. Based on their findings, they concluded that there is only a minimal influence of the frequency of vibration on the dynamic coefficients of a tilting-pad bearing. This is in apparent disagreement with the results of the present study. However, their experiments were limited to a narrow range of excitation frequencies, from 60% to 90% of the synchronous frequency, and relatively low speeds (the maximum speed was 3600 rpm). For example, the excitation frequency range for the maximum speed is from 36 to 54 Hz.

Certainly, if we limited the dynamic stiffness data of Fig. 21 to a frequency range of, say, 60-90 Hz, the conclusion would also be that the influence of the frequency of excitation is not significant. Therefore, a broad range of frequencies of excitation is essential for providing a complete description of the frequency-dependent characteristics of the dynamic coefficients of a TP bearing.

Rotordynamic calculations are based on linearized dynamic coefficients, which for bearings are customarily comprised of two 2x2 matrices of frequency-independent

stiffness and damping coefficients. However, we will include an added-mass matrix to the bearing model (Eq. 2) to account for the combined effects of the inertia of the fluid and the frequency dependency of the stiffness. This approach allows for the description of the bearing dynamic properties with three 2×2 *frequency-independent* linearized coefficient matrices.

As detailed in an earlier section, estimates for the rotordynamic coefficients are obtained by means of a least-squares linear regression of the dynamic stiffness data. Referring to Fig. 21, the real part of the direct dynamic stiffnesses ($\text{Re}(\mathbf{H}_{xx})$ and $\text{Re}(\mathbf{H}_{yy})$) is fitted to a line whose slope and intercept are estimates of the added-mass (M_{xx} , M_{yy}) and the stiffness (K_{xx} , K_{yy}) coefficients, respectively. Evaluating Eqs. 7(a) and 7(c) for $x_i = \Lambda_i$ and $y_i = \text{Re}(H_{xx_i})$, we obtain: $M_{xx}=38.3 \pm 2.5$ kg, and similarly $M_{yy}=35.6 \pm 6.2$ kg. By use of Equations 7(b) and 7(d), we obtain $K_{xx}=27.95 \pm 4.89$ MN/m and $K_{yy}=95.43 \pm 12.13$ MN/m.

In regards to the direct stiffness coefficients, note that K_{yy} is much larger than K_{xx} . This asymmetric is characteristic for a load-on-pad TP bearing, where the stiffness in the direction of the load is much larger than in the direction normal to it.

Fig. 22 presents the real part of the cross-coupled dynamic stiffness coefficients. In this case, some degree of frequency dependency is also observed. $\text{Re}(\mathbf{H}_{xy})$ has a negative sign and decreases with increasing frequency, whereas $\text{Re}(\mathbf{H}_{yx})$ is positive and increases. These results show the presence of cross-coupled added-mass terms of opposite sign.

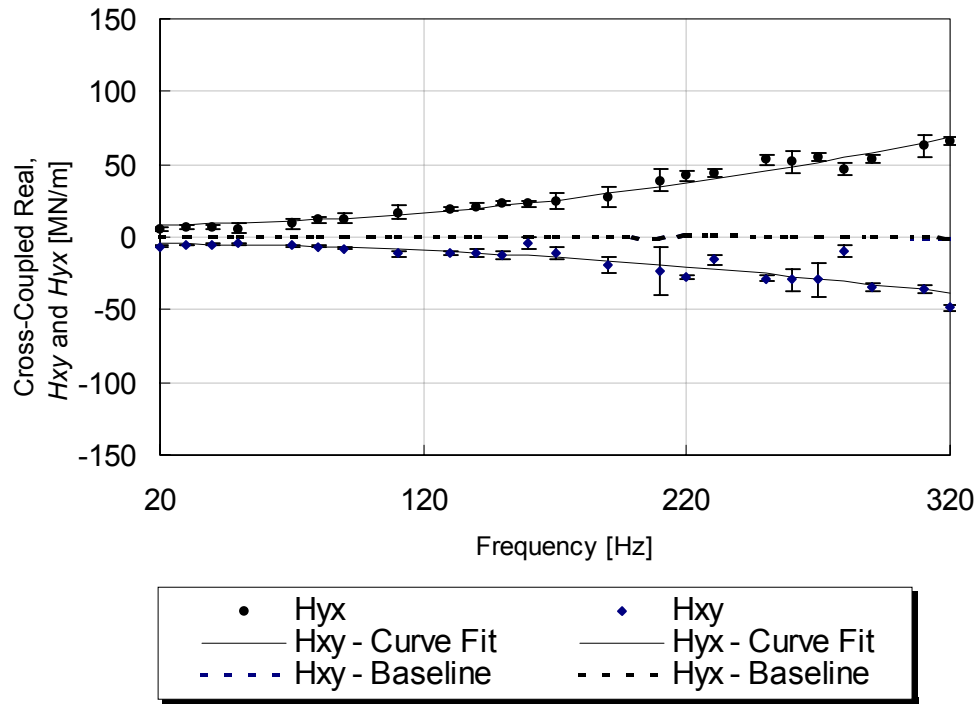


Fig. 22 Real cross-coupled dynamic stiffness at 6000 rpm and 689 kPa

We obtain the cross-coupled stiffness and the added-mass coefficients in a similar fashion as the direct terms, which yields:

$$\begin{aligned}
 M_{xy} &= 8.4 \pm 1.9 \text{ kg} & M_{yx} &= -15.1 \pm 1.2 \text{ kg} \\
 K_{xy} &= -4.49 \pm 4.89 \text{ MN/m} & K_{yx} &= 8.13 \pm 2.27 \text{ MN/m}
 \end{aligned}
 \tag{10}$$

In regard to the cross-coupled stiffness coefficients, for our coordinate system and sign convention (see Fig. 9), a positive K_{yx} term and a negative K_{xy} term act to destabilize a rotor, that is, they develop a reaction force that acts in the direction of the orbital motion of the rotor. When the damping available is not enough to cancel this “driving” force, the cross-coupled stiffness coefficients cause self-excited vibrations, and

the rotor becomes unstable. However, despite the presence of cross-coupled stiffness coefficients, FFTP bearings have excellent stabilizing characteristics (Zeidan and Paquette [1]).

Fig. 23 and Fig. 24 present the imaginary part of the direct and the cross-coupled dynamic stiffness, respectively.

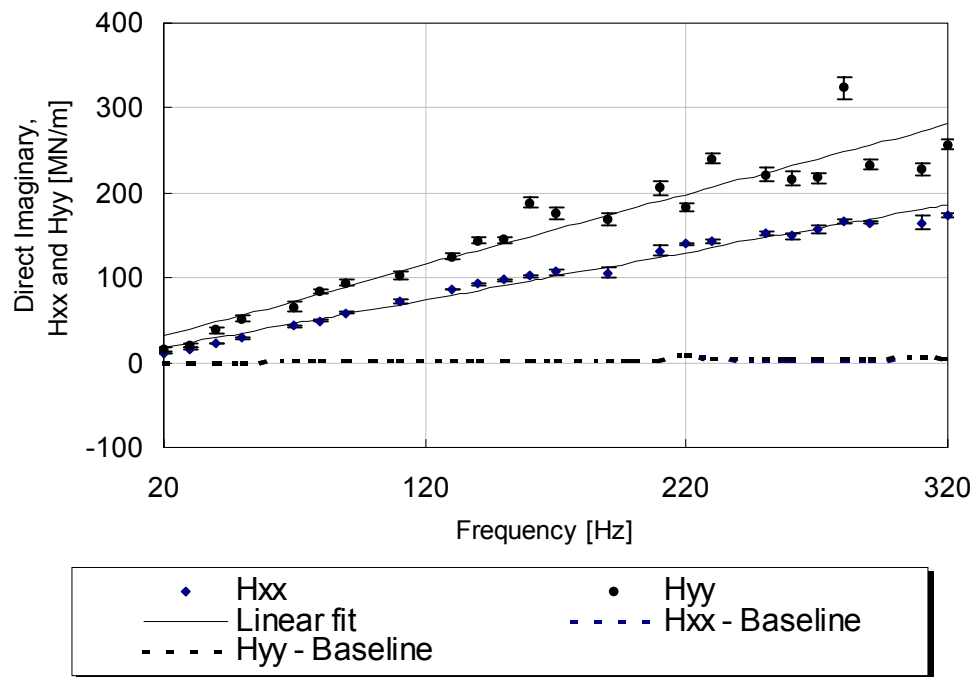


Fig. 23 Imaginary direct dynamic stiffness at 6000 rpm and 689 kPa

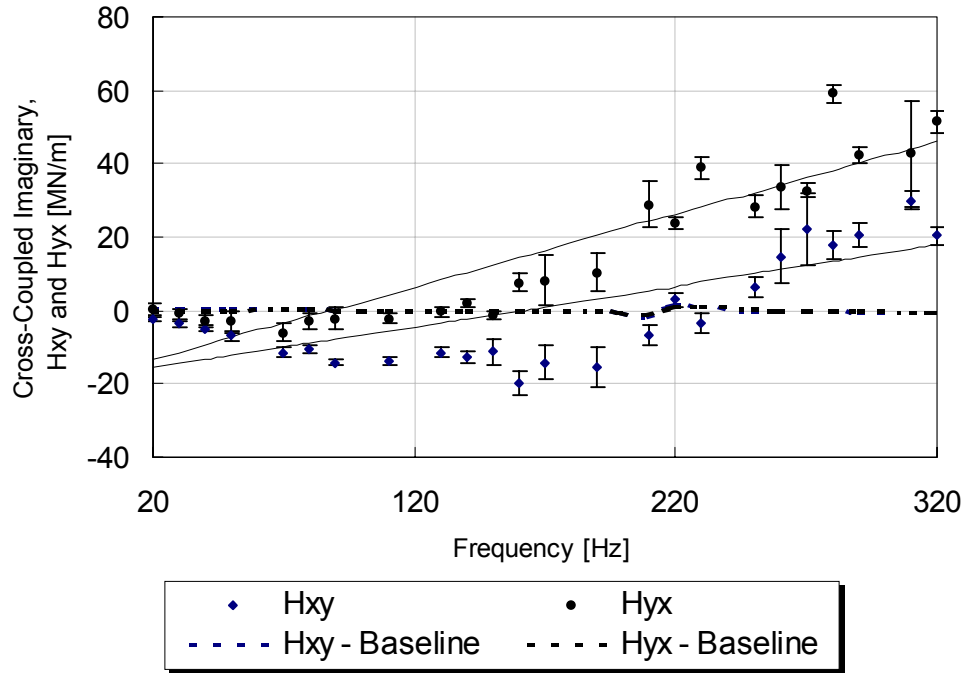


Fig. 24 Imaginary cross-coupled dynamic stiffness at 6000 rpm and 689 kPa

The damping coefficients (C_{xx} , C_{yy} , C_{xy} , C_{yx}) are identified from the slope of the imaginary parts of the dynamic stiffness. The intercept term is ignored in all cases. Eqs. 7(a) and 7(c) are evaluated for $x_i = \Omega_i$ and $y_i = \text{Im}(H_{xx_i})$. Thus we obtain:

$$\begin{array}{ll}
 C_{xx}=89.04\pm 5.01 & C_{xy}=17.65\pm 7.21 \\
 C_{yx}=31.56\pm 5.88 & C_{yy}=132.81\pm 17.54
 \end{array}
 \quad (\text{kN}\cdot\text{s}/\text{m}) \quad (11)$$

Note in Fig. 23 that the imaginary part of the dynamic stiffness tends to decrease slightly at higher frequencies (around 280 Hz for the case shown in the Figure), evidencing a small degree of frequency dependency for the damping coefficient. For most cases, this decrease starts at frequencies above the synchronous frequency. For this

reason, this frequency dependency is ignored and the damping is considered to be independent of frequency.

Fig. 25 shows the cross-coupled imaginary dynamic stiffnesses, which certainly do not follow a linear trend. Instead, they seem to increase with frequency in a higher order fashion. However, these values are much smaller than the direct imaginary dynamic stiffness. Therefore, a first order linear curve fit is used to obtain a rough approximation of the cross-coupled damping coefficients. This explains why large uncertainties are associated with these cross-coupled coefficients.

In addition to the uncertainties associated to each dynamic coefficient, the coefficient of determination (r^2 , commonly referred to as correlation factor) provides an indication of the goodness of the curve fits of experimental data. Large r^2 values indicate a good correlation between fit and data, with 1 being a perfect fit and zero meaning no correlation. The coefficients of determination for our example are shown in Table 4.

Table 4 Coefficients of determination for dynamic stiffness at 6000 rpm and 689 kPa

	Real	Imaginary
r^2_{xx}	0.9762	0.9822
r^2_{xy}	0.7747	0.5239
r^2_{yx}	0.9666	0.8341
r^2_{yy}	0.8499	0.9092

The description and discussion presented in this section is representative for most conditions of bearing load and rotor speed, and was provided as an example of the analysis and procedure to extract the rotordynamic data. The appendix contains the complete set of dynamic stiffness numerical data for all the test conditions listed in Table 2.

ROTOR DYNAMIC COEFFICIENTS

This section provides the results for the frequency independent rotordynamic coefficients as obtained in the preceding section. The experimental conditions presented here include three rotational speeds: 6000, 9000 and 13000 rpm, and three unit bearing loads: 172, 517 and 689 kPa.

Fig. 25 to Fig. 27 present the bearing stiffness, damping and added-mass coefficients matrices. Results are presented both as a function of unit load and of the shaft speed. Uncertainty bars are included for each individual point.

Note that the uncertainty in the direct coefficients in the direction of the load is generally larger than in the normal direction, because that the dynamic stiffness data in the y-direction are more scattered. This result has to do with the amplitude of motion of the bearing during shaking tests. The motion was somewhat limited in this direction because of the larger stiffness of the bearing, which renders smaller motions for a given shaking force. Smaller amplitudes of motion tend to provide larger signal-to-noise ratio, when compared to the larger motions in the normal direction, affecting the quality of the data.

Note that the rotordynamic coefficients for the rotational speed of 16000 rpm are not included in the plots. As pointed out in an earlier section, the oil temperature level at that speed was much higher than for the rest, which in turn made the viscosity much lower. Rotordynamic coefficients are strongly dependent on the viscosity of the fluid, therefore direct comparison of the coefficients for 16000 rpm with coefficients for the rest of the speeds may prove misleading. However, the numerical results for 16000 rpm are provided in the appendix, which contains both dynamic stiffness and rotordynamic coefficient data, for all test conditions.

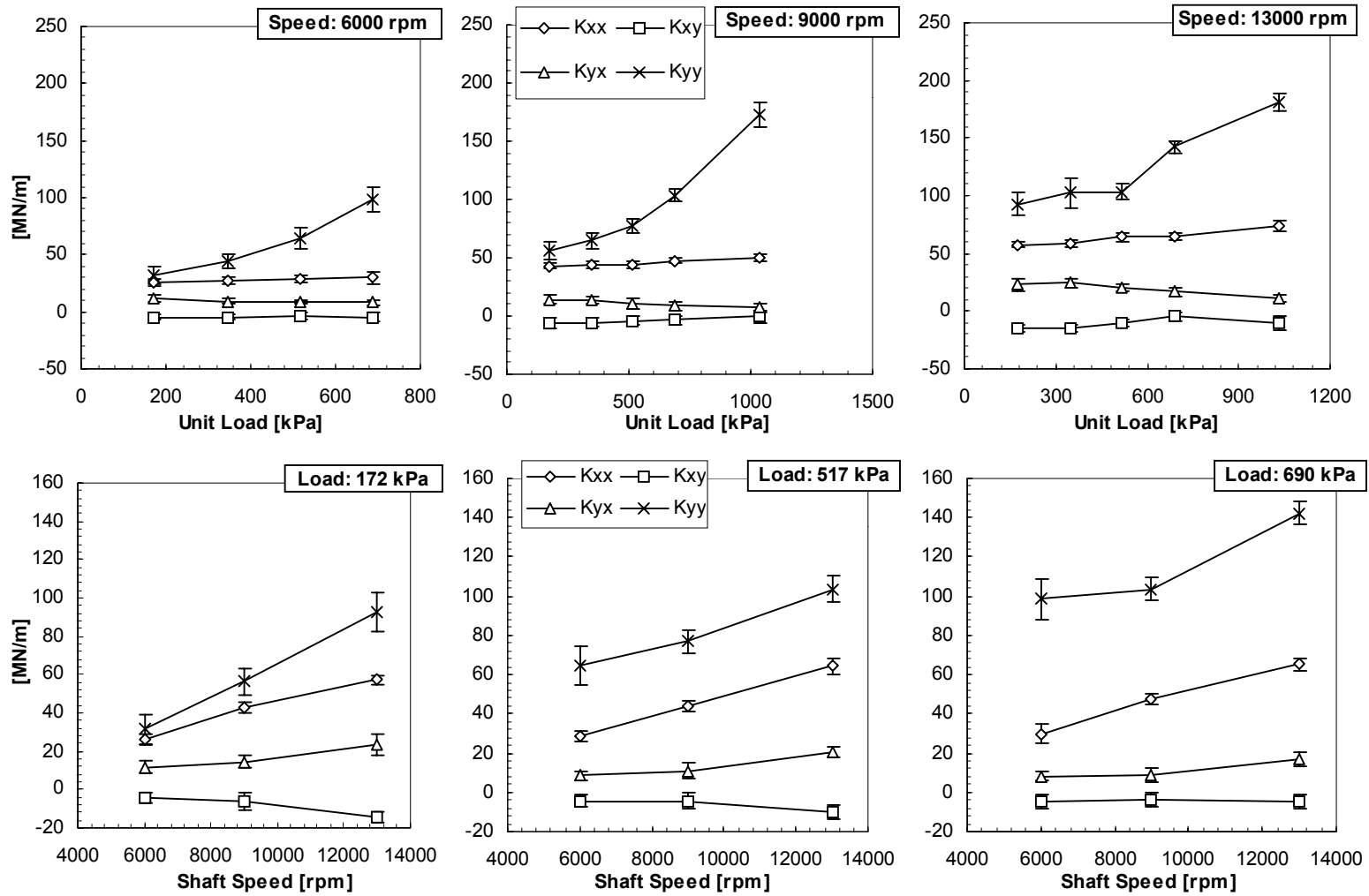


Fig. 25 Bearing stiffness coefficients

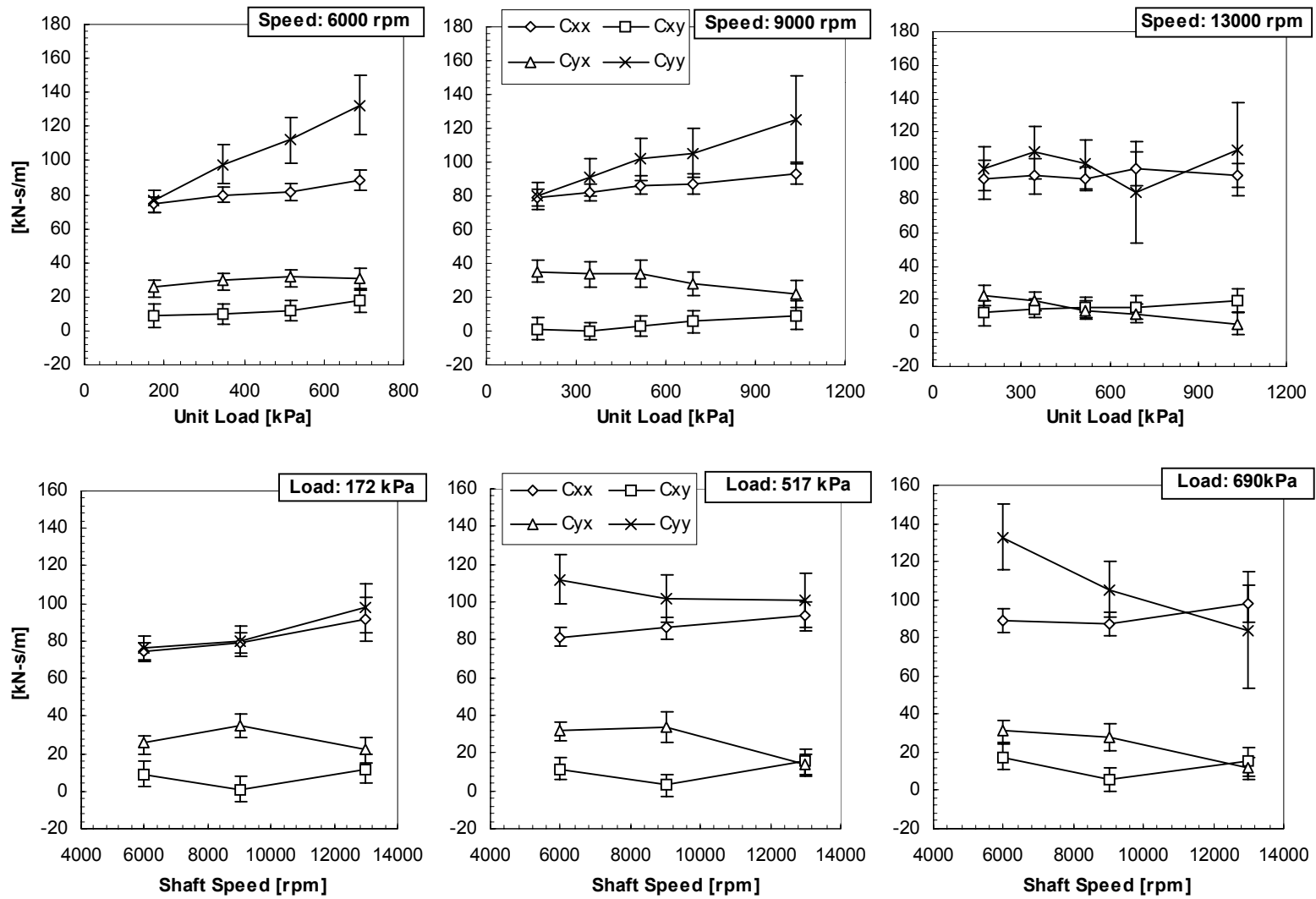


Fig. 26 Damping bearing coefficients

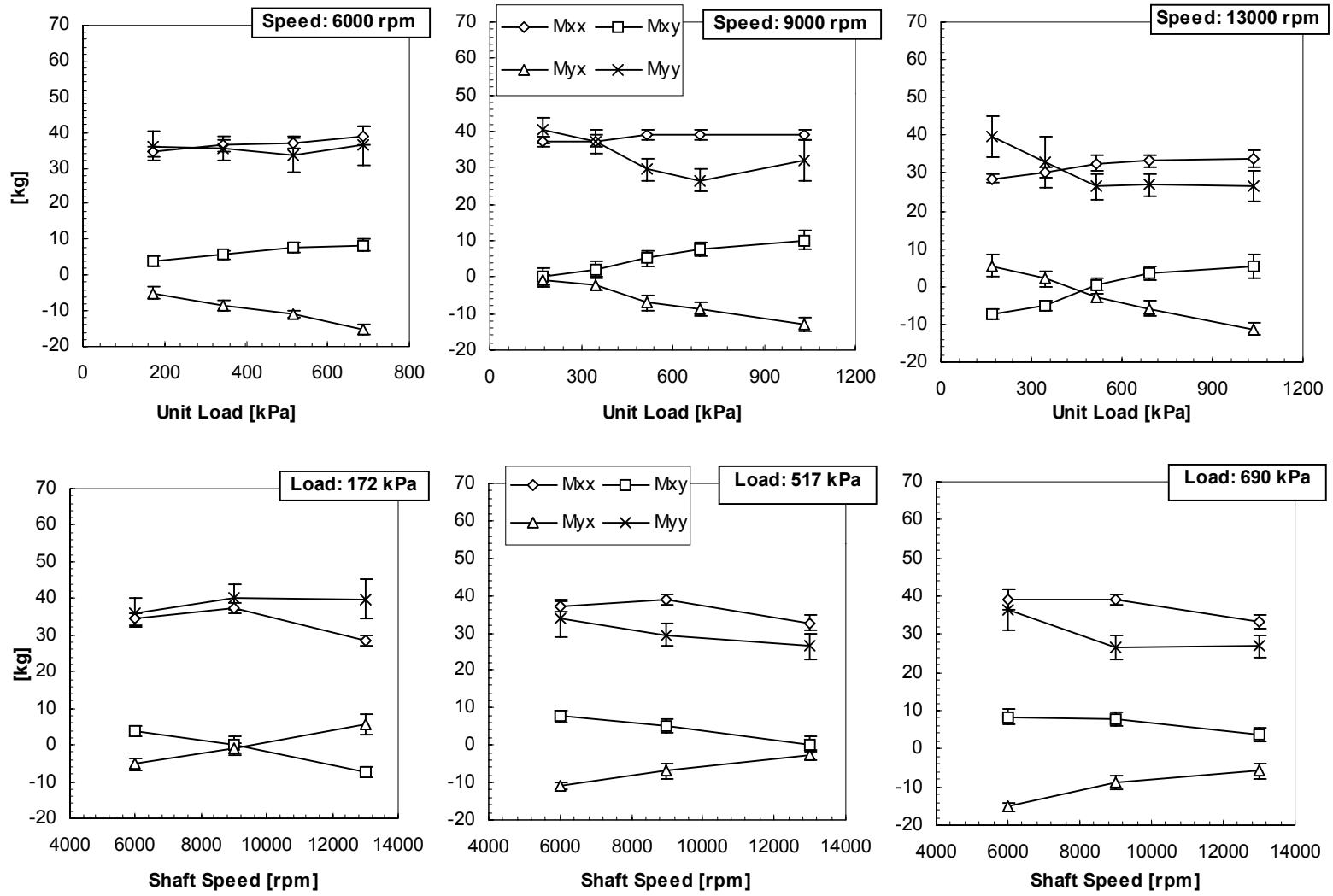


Fig. 27 Bearing added-mass coefficients

WHIRL-FREQUENCY RATIO

A commonly used parameter for evaluating the stability characteristics of a bearing is the whirl-frequency ratio (WFR). It is defined as the ratio between the rotor whirl (precessional) frequency and the speed at which the rotor-bearing system becomes unstable (referred to as “onset speed of instability”). The WFR is a stability indicator in that the higher the WFR the lower the onset speed of instability, and thus a less stable system. The formula used for WFR, was taken from San Andrés [20], and it includes the added-mass inertia coefficients.

Fig. 28 provides the whirl-frequency ratio as a function of the running speed and the bearing unit load. These results confirm the superior stability characteristics of a FPTP bearing when compared to a rigid geometry journal bearing, for which the WFR is typically 0.5.

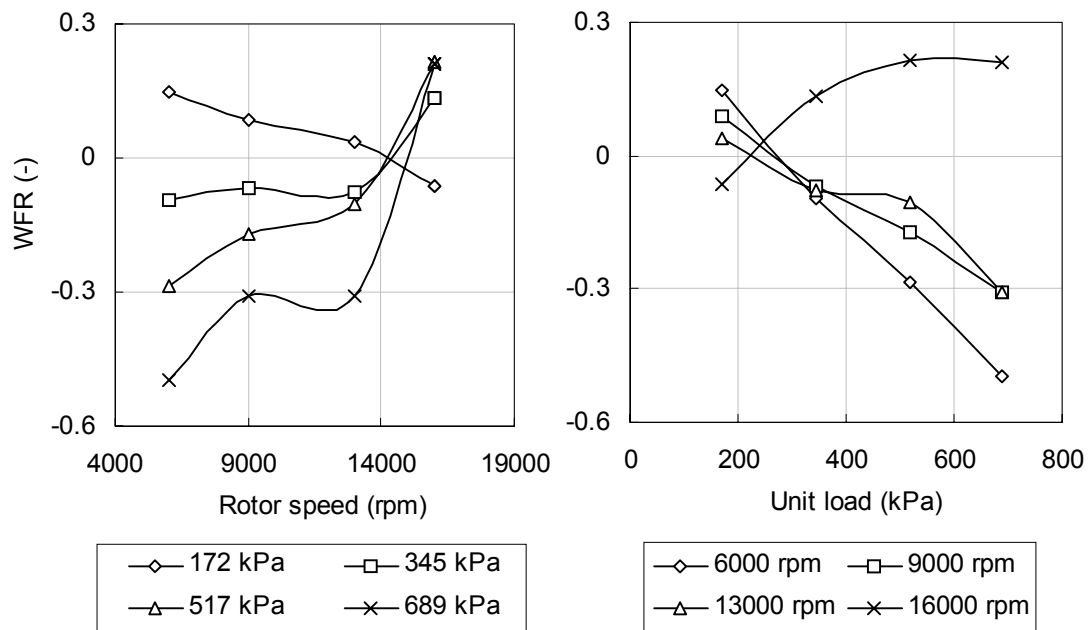


Fig. 28 Whirl-frequency ratio versus rotational speed (left) and unit load (right)

CHAPTER VIII

BULK-FLOW THEORY PREDICTIONS

FOREWORD

In the preceding chapter we presented strong experimental evidence to show the influence of the fluid inertial forces affects on the dynamic behavior of the FPTP bearing. Therefore, to accurately predict these results it is mandatory to use a theoretical model that accounts for fluid inertia for the prediction of stiffness and damping coefficients.

Classical lubrication theory relies on the Reynolds equation for the prediction of the pressure field inside the fluid film, and consequently the dynamic coefficients. The Reynolds equation is derived from the Navier-Stokes (NS) equations, by resorting to a series of assumptions related to the flow regime and the geometry (a very thin film of fluid). The Reynolds equation neglects the fluid inertia forces by dropping the temporal and convective acceleration terms from the momentum transport equations.

Reinhardt and Lund [5] explain that this is a justifiable assumption when the Reynolds number is small, on the order of one, but that for numbers in the order of 10^2 it ceases to be a correct assumption. The repercussion of this is that when the inertial terms are included in the first-order perturbation solution of the NS equations, the results show added-mass terms that can be several times the mass of the bearing journal. Incidentally, this same study showed that the stiffness and damping coefficients are only minimally affected by the fluid inertia.

The concept of added-mass coefficients in addition to stiffness and damping coefficients for bearings is not new in itself. Hybrid bearings (combination of hydrostatic and hydrodynamic) operate at very high Reynolds numbers and thus well in the turbulent regime, due to high speeds, elevated pressure-driven axial flow and low viscosity fluids. It follows that fluid inertia plays an important role in such application, and therefore it

becomes mandatory to use a solution of the NS equations including inertial forces to predict the added-mass coefficients.

San Andres [10] addressed this issue with a CFD (computational fluid dynamics) scheme for solving a bulk-flow version of the Navier-Stokes equations, to predict the static and dynamic characteristics of turbulent hybrid bearings. Perturbation of the flow and momentum conservation bulk-flow equations is used to calculate zeroth and first order flow fields, including the temporal and convective acceleration terms. This approach has been used with success in comparison to experimental results obtained for a hybrid bearing (Franchek et al. [11]).

San Andres [6] later presented an extension of this bulk-flow model to analyze FPTP and conventional TP fluid film bearings. The computer code, XLTFPBrg - available with the Turbomachinery Laboratory's Rotordynamic Software Suite, will be used here to generate theoretical predictions for dynamic stiffness of the FPTP bearing.

Information required for the model/computer code consists of bearing geometry, pad inertia and rotational stiffness, load orientation, operating conditions (speed and load), lubricant characteristics, and thermal model. For the predictions shown here, the isothermal (constant viscosity) model was chosen for simplicity mainly. Trial runs were made using the adiabatic model (no heat conduction to the bearing or journal), and found only minor differences in the rotordynamic coefficients.

DYNAMIC STIFFNESS

Fig. 29 shows the real part of the direct dynamic stiffness of the bearing at a speed of 9000 rpm and a unit load of 690 kPa. Two solutions have been included, a) solution of the NS bulk-flow equations including temporal and convective acceleration terms (in solid lines and denoted as "full inertial"), and b) the NS bulk-flow equations ignoring these terms which reduces to the Reynolds equation solution (in dashed lines and denoted as "inertialess").

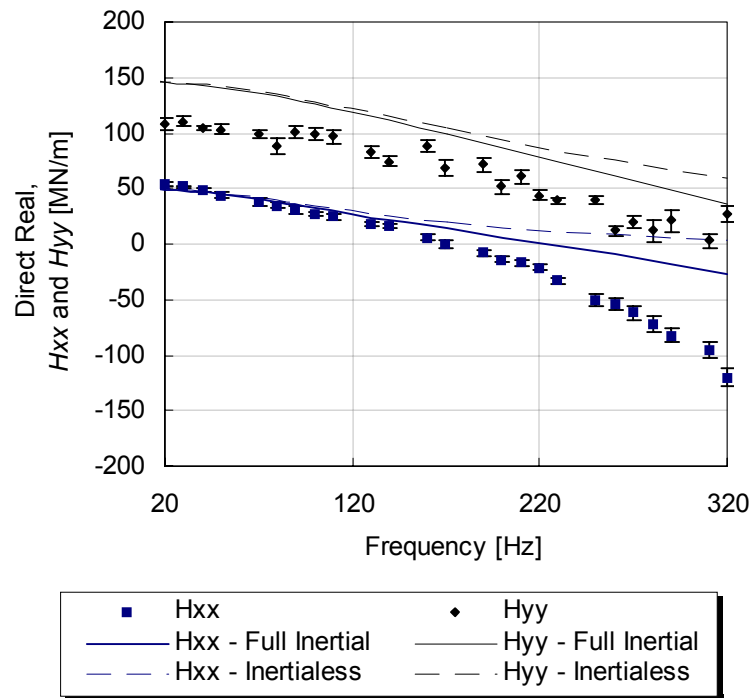


Fig. 29 Predicted real part of H_{xx} and H_{yy} , 9000 rpm and 689 kPa

The full inertial solution for $\text{Re}(H_{xx})$ and $\text{Re}(H_{yy})$ predicts a frequency dependency similar to the measurements. For $\text{Re}(H_{xx})$, the agreement is very good at low frequencies; whereas, the measurements show the dynamic stiffness to decrease much faster than the theory predicts. This means that the theory under predicts the added mass term (M_{xx}). About $\text{Re}(H_{yy})$, the theory generally over predicts the stiffness, as in this particular case. However, note how the rate in which the $\text{Re}(H_{yy})$ decreases is fairly similar for both theory and experiment, which indicates a good prediction of M_{yy} .

The results for the inertialess solution (Reynolds equation) show the isolated effect of the frequency dependency of the dynamic stiffness coefficients due to the degrees of freedom of the pads. The full inertial solution shows the additional effect of the inertia terms. These results confirm that the frequency dependency observed in experimental results is due to both effects combined.

A convenient way to reduce the results presented in Fig. 29 is to use an added-mass term to account for the frequency dependency by estimating the added-mass coefficients with the same curve fit procedure detailed in an earlier section.

Here, the intercepts, K_{xx} and K_{yy} , may be obtained from the low frequency values (5 Hz) instead. This approach is convenient because it will produce a rotordynamic-coefficient bearing model that is independent of the frequency of vibration. Clearly, such a representation is very attractive as it eliminates the question whether the reduced stiffness coefficients must be calculated at the synchronous frequency or some other frequency. In a nutshell, the low frequency value of the dynamic stiffness provides the stiffness of the bearing, and an added-mass term accounts for the frequency dependency of the dynamic stiffness.

Table 5 shows the numerical values of the coefficients reduced from the theoretical dynamic stiffness. As expected from our discussion, agreement between experiment and the inertial solution is the best, specifically for the added-mass coefficients. In terms of stiffness coefficients, both theoretical models yield similar results.

Table 5 Predicted stiffness and added-mass coefficients, 9000 rpm and 689 kPa

		Kxx	Kyy	Mxx	Myy
		MN/m		kg	
	Full Inertial	49.87	143.81	19.45	28.16
	Inertialess	43.77	137.56	12.22	22.67
	Experiment	46.78	105.85	38.24	29.09
percent difference	Full Inertial	-6.20%	-26.4	96.60%	3.30%
with experiments:	Inertialess	6.90%	-23.10%	212.90%	28.30%

Fig. 30 shows the imaginary part of the direct dynamic stiffness for the same condition. Only the full inertial solution is included as the fluid inertia has a negligible

effect on $\text{Re}(H_{yx})$, $\text{Re}(H_{xy})$ and $\text{Im}(H_{ij})$. Again, the agreement is excellent, especially at frequencies up to the synchronous frequency (150 Hz).

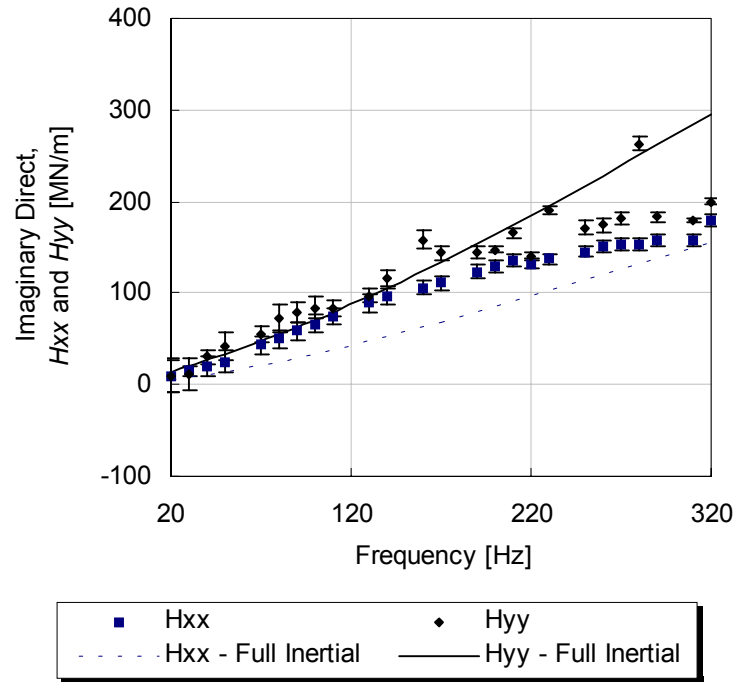


Fig. 30 Predicted imaginary part of H_{xx} and H_{yy} , 9000 rpm and 689 kPa

Consequently, the damping coefficients identified from these results also show good agreement with measurements, as shown in Table 6. The damping coefficients predictions given here are calculated at the synchronous frequency (150Hz).

Table 6 Predicted direct damping coefficients, 9000 rpm and 689 kPa

	Cxx	Cyy
	kN.s/m	
Full Inertial	61.39	118.91
Experiment	87.68	108.59
% difference	42.80%	-8.70%

Fig. 31 shows the real part of the cross-coupled dynamic stiffness for the full inertial solution. Both $\text{Re}(H_{xy})$ and $\text{Re}(H_{yx})$ agree well with experiments from low frequencies up to the synchronous frequency (150 Hz). At larger frequencies the theoretical values decrease in magnitude whereas the experiments show the opposite. Accordingly, the model does not correctly predict the cross-coupled added-mass coefficients.

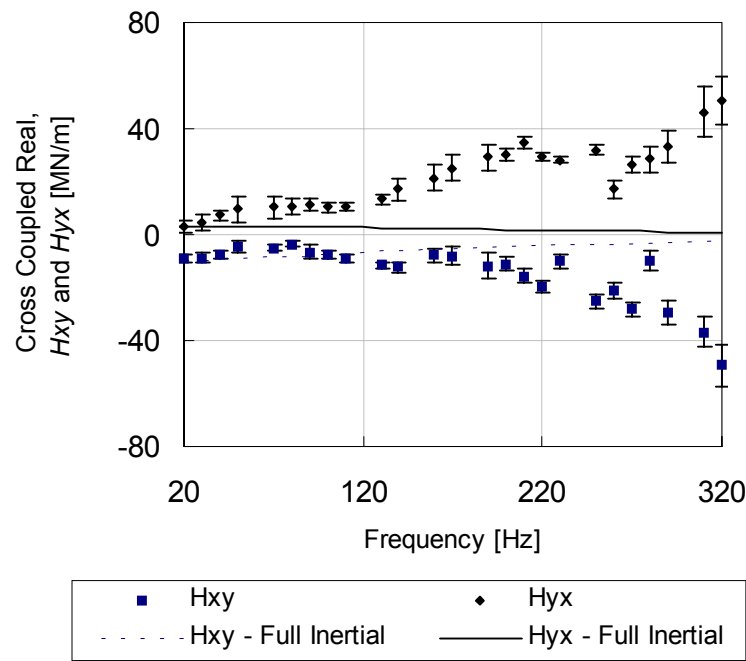


Fig. 31 Predicted real part of H_{xy} and H_{yx} , 9000 rpm and 689 kPa

Concerning the prediction of the K_{yx} and K_{xy} , the agreement with experiments is only fair, as shown by Table 7. As with the direct terms, predictions for K_{xy} and K_{yx} are taken simply from the lowest frequency value (5 Hz) of the real part of the cross-coupled dynamic stiffnesses, $\text{Re}(H_{xy})$ and $\text{Re}(H_{yx})$. The added-mass coefficients are obtained from the curve-fit. First, the code predicts added-mass terms that are an order of

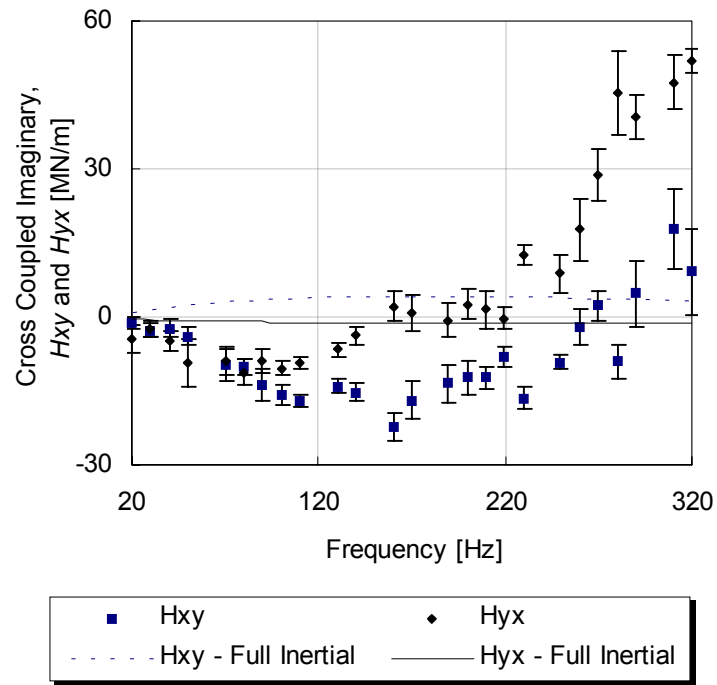
magnitude smaller. Additionally, the trends of the dynamic stiffnesses are the opposite, e.g., while $\text{Re}(\mathbf{H}_{yx})$ decreases with increasing vibration frequency (evidencing a positive cross-coupled added mass term), the theory predicts that it increases, which in turn is related to the presence of a negative added-mass term.

Table 7 Predicted cross-coupled stiffness coefficients, 9000 rpm and 689 kPa

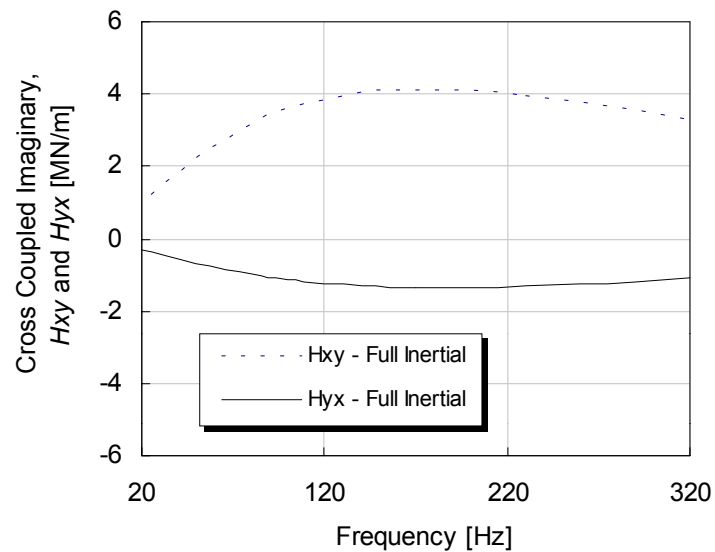
	Kxy kN.s/m	Kyx	Mxy kN.s/m	Myx
Full Inertial	-9.64	3.3	-1.82	0.61
Experiment	-4.84	9.13	6.28	-8.36
% difference	-49.80%	177.10%	-445.10%	1470.50%

Fig. 32 presents the imaginary part of the cross-coupled dynamic stiffnesses for the same condition as in the previous figures. The comparison with the experimental measurements is poor. The predictions are one order of magnitude less than the measurements. Also, the experimental $\text{Im}(\mathbf{H}_{yx})$ and $\text{Im}(\mathbf{H}_{xy})$ follow the same trend and have the same sign, whereas the predictions have a different sign, as shown in Fig. 33 (b). The predicted cross-coupled damping coefficients calculated at the synchronous frequency were used for comparison with the experimental coefficients.

(a) Theory vs. experiment



(b) Theory only

Fig. 32 Predicted imaginary part of H_{xy} and H_{yx} , 9000 rpm and 689 kPa

PREDICTED ROTORDYNAMIC COEFFICIENTS

Predictions for rotordynamic coefficients are presented as an example for a rotational speed of 13000 rpm and a bearing load of 345 kPa.

Fig. 33 shows the stiffness coefficients for a rotational speed of 13000 rpm and a bearing unit load of 345 kPa. As explained earlier, the direct and cross-coupled stiffness coefficients are extracted from the real part of the dynamic stiffness at a low frequency (5 Hz), rather than from the linear curve-fit. This approach is taken because the theoretical dynamic stiffness does not produce a perfect a parabola, particularly at low frequencies which can induce considerable error, if the stiffness coefficients were obtained from the intercept of the curve fit.

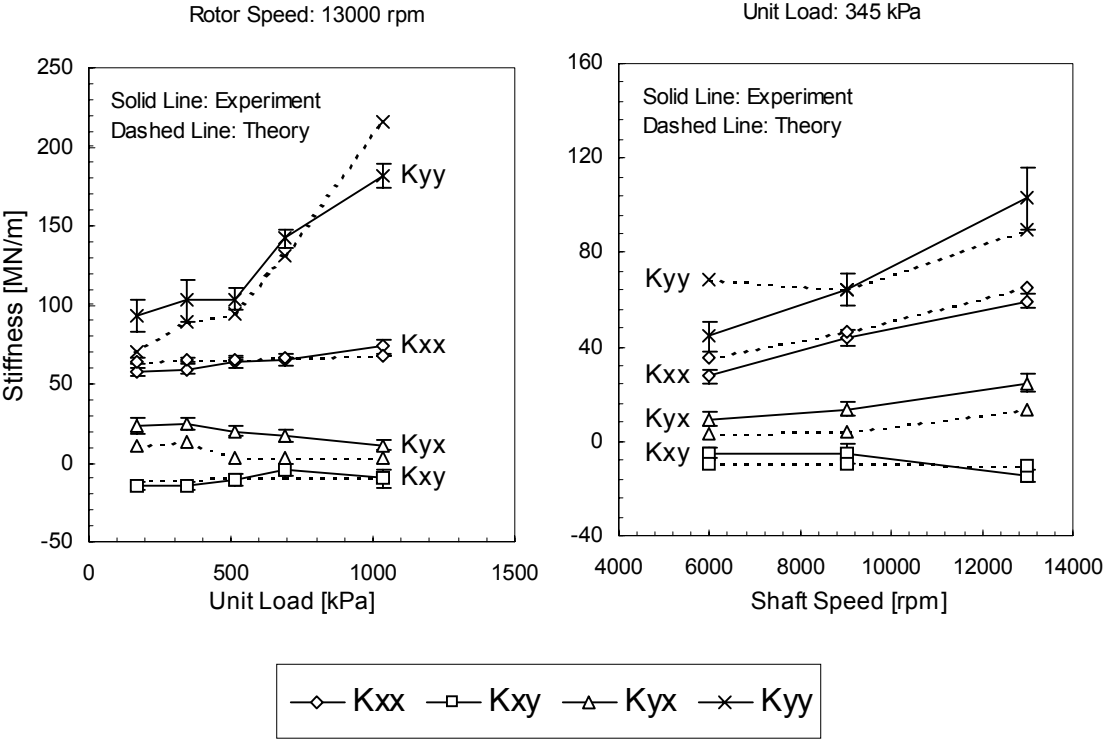


Fig. 33 Stiffness coefficients - theory versus experiment

The agreement with the experimental coefficients is very good overall, and this is the case for all speeds. For the direct coefficients, agreement is certainly better for K_{xx} than for K_{yy} . This is perhaps due to an asymmetry in the actual bearing clearance, probably caused by the press-fit between the bearing and the retainer. This condition is often referred to as *bearing crush*. For the cross-coupled coefficients, agreement is very good for K_{xy} , although K_{yx} is underpredicted by a factor of 3 for most conditions.

Fig. 34 presents the predicted and measured damping coefficients. The comparison here is not so satisfactory since C_{xx} is underpredicted by a 67% for most cases. Agreement for C_{yy} is slightly better, considering the larger level of uncertainty in this coefficient. As we had anticipated, the prediction of the cross-coupled terms is rather poor. Their magnitudes are underpredicted and the sign of C_{yx} is not correct.

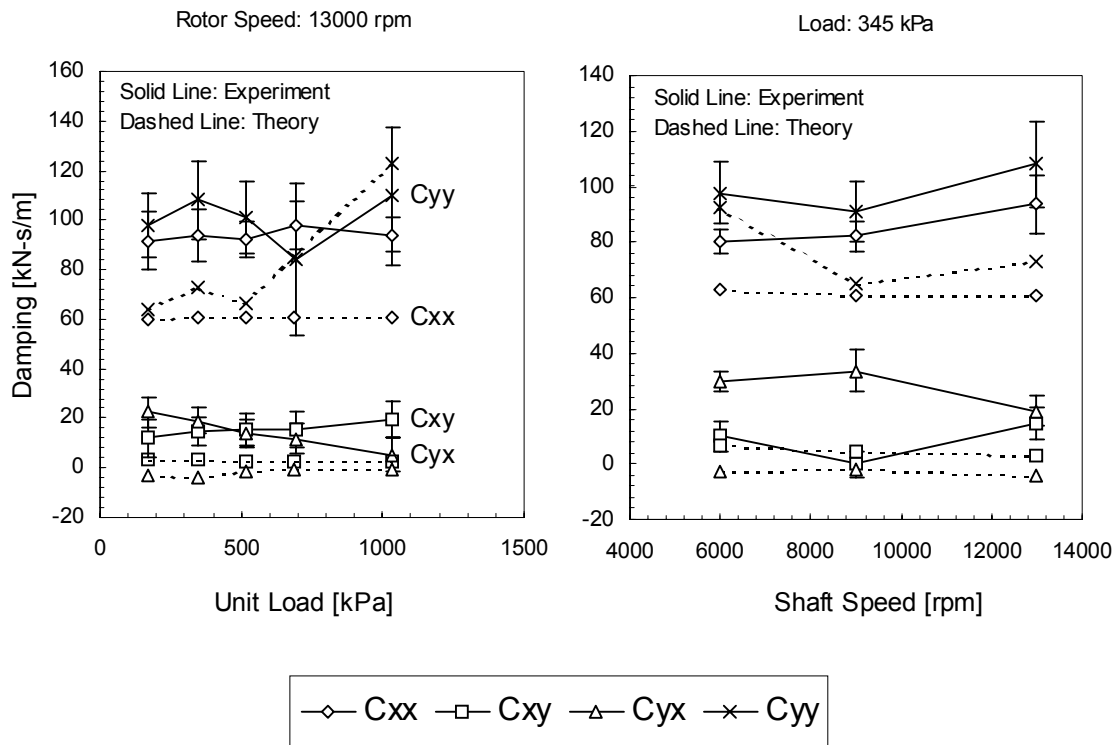


Fig. 34 Damping coefficients - theory versus experiment

Fig. 35 presents the added-mass coefficients. The theory does a fair job in predicting the added-mass coefficients. M_{xx} is generally underpredicted between 50 and 60 percent. Agreement for M_{yy} is excellent, specially at large loads (high eccentricity). The magnitude of the cross-coupled terms is generally under predicted, although the code correctly predicts they have opposite signs.

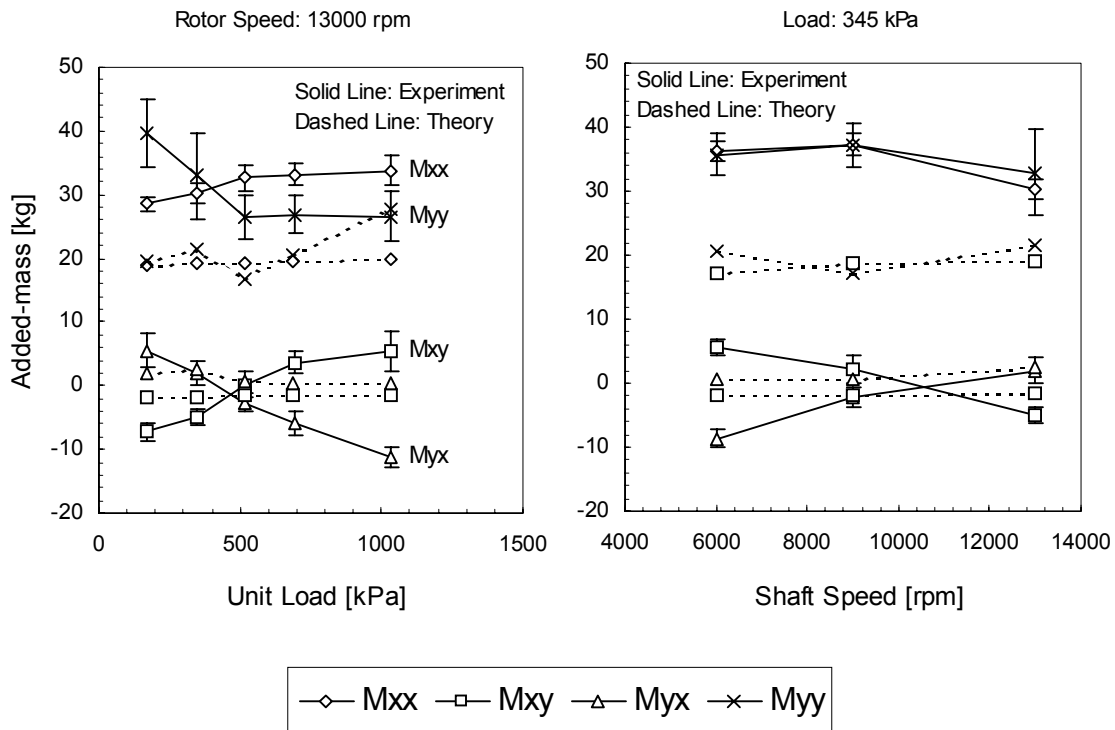


Fig. 35 Added-mass coefficients - theory versus experiment

CHAPTER IX

CONCLUSIONS AND RECOMMENDATIONS

This thesis provides experimental results of frequency-dependent stiffness and damping coefficients results for a four pad, high-speed, load-on-pad, flexible-pivot tilting pad bearing. Test conditions include four shaft rotational speeds from 6000 to 16000 rpm and bearing unit loads from 172 to 1034 kPa. Steady-state performance measurement results are also presented, including pad metal temperatures, eccentricity ratios and attitude angles as a function of bearing load, and estimated frictional power losses.

Dynamic performance results show that the stiffness coefficients are strongly dependent upon the frequency of excitation. This outcome is due to two combined effects. First, frequency dependency is introduced by the dynamics of the additional degree of freedom of the pads (as compared to a rigid geometry bearing). Second, inertial forces of considerable magnitude are generated in the fluid films for all test conditions. This frequency dependency is well modeled with an added-mass matrix, producing three 2×2 *frequency-independent* matrices of stiffness, damping and added-mass. This approach resolves the question of whether the TP bearing dynamic coefficients should be calculated at the synchronous frequency or some other frequency, as is the common practice when performing rotordynamic calculations.

The experimental findings are compared to predictions generated with a bulk-flow solution of the Navier-Stokes (NS) equations that includes the temporal and convective acceleration terms. The model yields predictions that are in good agreement with the experimental measurements. Additionally, the results are compared to predictions based on the Reynolds equation. The bulk-flow NS model provides better predictions for the added-mass coefficients, because it accounts for the fluid inertial forces.

Using the Reynolds equation and consequently neglecting the effect of the fluid inertia has here been proven to be inadequate to accurately predict the dynamic behavior of tilting-pad bearings. Therefore, a solution of the Navier-Stokes equations that retains the temporal and convective acceleration terms should be used to calculate the rotordynamic coefficients of a flexible-pivot tilting-pad bearing.

Depending upon the geometric characteristics and operating conditions of the bearing, the direct added-mass coefficients may be significant and impact rotor dynamics predictions for light machines. Analyses must be made on a case-by-case basis to determine whether the added-mass coefficients are needed to obtain sufficient accuracy in rotordynamic calculations of critical speeds and instability margins.

Rotordynamic analyses are recommended, including bearing added-mass terms, for: 1) a machine supported in similar bearings to the one studied here, such as a multi-stage centrifugal compressor; and 2) a light, high-speed machine, such as an integrally geared compressor. These analyses will provide insight on the impact of the bearing added-mass coefficients on rotor dynamics of machines supported on flexible-pivot tilting-pad bearings.

REFERENCES

- [1] Zeidan, F. and Paquette, D., 1994, "Application of High Speed and High Performance Fluid Film Bearings in Rotating Machinery" *Proceedings of the 23rd Turbomachinery Symposium*, Turbomachinery Laboratory, Texas A&M University, pp. 209-233.
- [2] Armentrout, R., and Paquette, D., 1993, "Rotordynamic Characteristics of Flexure-Pivot Tilting-Pad Journal Bearings," *Tribol. Transactions*, **36**, 3, pp. 443-451.
- [3] Lund, J., 1964, "Spring and Damping Coefficients for the Tilting-Pad Journal Bearing," *ASLE Transactions*, **7**, pp. 342-352.
- [4] Barret, L., Allaire, P., and Wilson, B., 1988, "The Eigenvalue Dependence of Reduced Tilting Pad Bearing Stiffness and Damping Coefficients," *Tribol. Transactions*, **31**, 4, pp. 411-419.
- [5] Reinhardt, E., and Lund, J., 1975, "The Influence of Fluid Inertia on the Dynamic Properties of Journal Bearings," *ASME J. of Lubrication Technology*, **97**, pp. 159-167.
- [6] San Andrés, L., 1996, "Turbulent Flow, Flexure-Pivot Hybrid Bearings for Cryogenic Applications," *ASME J. of Tribol.*, **118**, pp. 190-200.
- [7] Nicholas, J., Gunter, E., and Allaire, P., 1978, "Stiffness and Damping Coefficients for the Five-Pad Tilting-Pad Bearing," *ASLE Transactions*, **22**, 2, pp. 113-124.
- [8] Ha, H., and Yang, S., 1999, "Excitation Frequency Effects the Stiffness and Damping Coefficients of a Five –Pad Bearing Tilting Pad Bearing," *ASME J. of Tribol.*, **121**, pp. 517-522.
- [9] Chen, W., 1995, "Bearing Dynamic Coefficients of Flexible-Pad Journal Bearings," *Tribol. Transactions*, **38**, 2, pp. 253-260.
- [10] San Andrés, L., 1990, "Turbulent Hybrid Bearings With Fluid Inertia Effects," *ASME J. of Tribol.*, **112**, pp. 699-707.

- [11] Franchek, N., Childs, D., and San Andres, L., 1995, "Theoretical and Experimental Comparisons for Rotordynamic Coefficients of a High-Speed, High-Pressure, Orifice-Compensated Hybrid Bearing" ASME J. of Tribol., **117**, pp. 285-290.
- [12] Pettinato, B. and De Choudhury, P., 1999, "Test Results of Key and Spherical Pivot Five-Shoe Tilt Pad Journal Bearings-Part I: Performance Measurements" Tribol. Transactions, **42**, 3, pp. 541-547.
- [13] De Choudhury, P., Hill, M., and Paquette, D., 1992, "A Flexible Pad Bearing System for a High Speed Centrifugal Compressor," *Proceedings of the 21st Turbomachinery Symposium*, Turbomachinery Laboratory, Texas A&M University, pp. 57-64.
- [14] San Andrés, L., and Jackson, M., 1998, "Measurements of the Static Load (On Pad) Performance and Pad Temperatures in a Flexure-Pivot Tilting-Pad Bearing" Tribol. Transactions, **41**, 2, pp. 225-232.
- [15] Kaul, A., 1999, "Design and Development of a Test Setup for the Experimental Determination of the Rotordynamic and Leakage Characteristics of Annular Bushing Oil Seals," M.S. Thesis, Mechanical Engineering, Texas A&M University.
- [16] Childs, D., and Hale, K., 1994, "A Test Apparatus and Facility to Identify the Rotordynamic Coefficients of High-Speed Hydrostatic Bearings," ASME J. of Tribol., **116**, pp. 337-344.
- [17] Rouvas, C., and Childs, D., 1993, "A Parameter Identification Method for the Rotordynamic Coefficients of a High Reynolds Number Hydrostatic Bearing," ASME J. of Vibration and Acoustics, **115**, pp. 264-270.
- [18] Montgomery, D.C. and Runger, G.C., 2003, *Applied Statistics and Probability for Engineers*, 3rd Edition, John Wiley and Sons, New York.
- [19] Bouchoule, C., Fillon, M., Nicholas, D., and Barresi, F., 1996, "Experimental Study of Thermal Effects in Tilting-Pad Journal Bearings at High Operating Speeds," ASME J. of Tribol., **118**, pp. 532-538.
- [20] San Andres, L., 1991, "Effect of Eccentricity on the Force Response of a Hybrid Bearing," Tribol. Transactions, **34**, 4, pp. 537-544.

APPENDIX

This appendix contains additional numerical data and plots of dynamic stiffness and rotordynamic coefficients, including uncertainties for the experimental conditions listed in Table 2. These data can be found in the accompanying spreadsheet file.

VITA

Luis Emigdio Rodriguez Colmenares, the son of Emigdio Rodriguez and Vilma Colmenares, was born on January the 20th, 1978, in the city of Valencia, Venezuela. He started his undergraduate studies at the Universidad Simón Bolívar (Caracas, Venezuela) in 1995, where he graduated as a Mechanical Engineer on January 19th, 2001. He performed his undergraduate thesis work during his stay as an exchange student at the Rotordynamics Laboratory of Texas A&M University (TAMU) in College Station, Texas. Shortly after graduation, he was accepted to TAMU to pursue a Master's of Science degree in Mechanical Engineering. There, he worked at the Turbomachinery Laboratory as a research assistant, investigating the rotordynamic coefficients and steady-state performance of tilting-pad bearings and laminar oil seals.

Permanent address:

Residencias Macarena, Apartamento 4-C
Urbanización El Bosque, Calle Los Robles
Valencia, Estado Carabobo
Venezuela